OPEN ACCESS
IOP Publishing | ISECAEP
Journal of Reliability Science and Engineering
J. Reliab. Sci. Eng. **2** (2026) 035501 (29pp)
https://doi.org/10.1088/3050-2454/ae885a

Dynamic reliability framework for resilience assessment for floating offshore wind turbines

Zifei Xu[1,2,3,*], Huahao Ou[3], Musa Bashir[2], Michael Beer[2,4,5], Jin Wang[1] and Zaili Yang[1,*]

[1] Liverpool Logistics Offshore and Marine Research Institute, Liverpool John Moores University, Liverpool, United Kingdom
[2] Department of Civil and Environmental Engineering, University of Liverpool, Liverpool, United Kingdom
[3] School of Power and Energy Engineering, University of Shanghai for Science and Technology, Shanghai, People's Republic of China
[4] Institute for Risk and Reliability, Leibniz University Hannover, Hannover, Germany
[5] International Joint Research Centre for Resilient Infrastructure & International Joint Research Centre for Engineering Reliability and Stochastic Mechanics& Tongji University, Shanghai, People's Republic of China

E-mail: z.xu@ljmu.ac.uk and z.yang@ljmu.ac.uk

Received 9 June 2026, revised 23 June 2026
Accepted for publication 8 July 2026
Published 21 July 2026

Abstract

Floating offshore wind turbines (FOWTs) are becoming an important part of future energy systems and can complement conventional energy grids in supporting overall energy safety and security. Understanding the dynamic reliability evolution of FOWTs under hazardous events and degradation-induced failures remains largely unexplored and represents a major scientific challenge. Existing monitoring systems, such as SCADA, have limited capability to identify the true root causes of component-level failures. Consequently, maintenance actions may target incorrect or incomplete failure sources, while undetected root causes may continue to propagate residual damage and accelerate degradation of other components. This study develops a dynamic reliability assessment framework for resilience-oriented recovery management of FOWTs under hazardous conditions. A Bayesian network is employed to represent the hierarchical FOWT system and model the propagation of component-level failures to subsystem- and system-level functionality degradation. During recovery, the framework captures the effects of residual damage from unidentified or incompletely repaired root failures on subsequent reliability evolution. A condition-aware deep inspection module is introduced to represent a PHM-enabled recovery process. Although this strategy requires additional inspection effort and decision-making resources before maintenance, it can more accurately identify root causes and propagation pathways, supporting more effective recovery decisions. A case study demonstrates that system reliability can decrease rapidly when critical components are affected by hazardous events. It further shows that experience-based recovery can partially

* Authors to whom any correspondence should be addressed.

Original content from this work may be used under the terms of the Creative Commons Attribution 4.0 licence. Any further distribution of this work must maintain attribution to the author(s) and the title of the work, journal citation and DOI.

© 2026 The Author(s). Published by IOP Publishing Ltd on behalf of the Institute of Systems Engineering, China Academy of Engineering Physics

restore system functionality but may fail to eliminate residual damage when root causes are not fully identified. In contrast, the condition-aware strategy achieves greater reliability restoration by improving root-cause identification and repair effectiveness. The results reveal the importance of integrating condition-aware inspection into post-disaster recovery planning and highlight the value of dynamic reliability assessment for resilience improvement in FOWTs. Specifically, the study provides a quantitative understanding of how PHM performance influences recovery effectiveness and resilience improvement, thereby supporting the evaluation of PHM value in post-disaster recovery management of FOWTs.

Keywords: floating offshore wind turbines, Bayesian network, condition-aware recovery, energy infrastructure resilience, prognostics and health management

Nomenclature

FOWT	Floating offshore wind turbine
BN	Bayesian network
DBN	Dynamic Bayesian network
CPT	Conditional probability table
RI	Reliability index
DRI	Dynamic reliability index
PHM	Prognostics and health management
BM	Benchmark (Strategy)
OR	Oracle (Strategy)
SCADA	Supervisory control and data acquisition
$\mathcal{G}$	Directed acyclic graph
V	Set of nodes in the graph
$\mathcal{E}$	Set of directed edges in the graph
$\mathcal{B}$	Set of root-level failure nodes
A	Set of observable abnormal nodes
$\mathcal{S}$	Set of sub-system nodes
$\mathcal{F}$	Top-level FOWT malfunction node (or its random variable)
$n_{\mathcal{B}}$	Total number of root-level failure nodes
$n_{\mathcal{A}}$	Total number of observable abnormal nodes
n_S	Total number of sub-system nodes
B_i	Random variable of the ith root-level failure node
A_j	Random variable of the jth abnormal manifestation
S_k	Random variable of the kth sub-system node
X_l	An arbitrary node variable in the Bayesian network
$\mathbb{X}_{\mathcal{V}}$	Collection of random variables associated with all nodes in $\mathcal{V}$
$\mathrm{pa}_{\mathcal{G}}(X_l)$	Parent-node set of nodes X_l in the directed graph
$\mathbb{X}_{\mathrm{pa}_{\mathcal{G}}(X_l)}$	Random variables associated with the parent nodes of X_l
$x_{\mathrm{pa}_{\mathcal{G}}(A_j)}$	A specific state configuration of the parent nodes of A_j
$\lambda_i(t)$	Time-dependent prior failure rate of root node B_i
λ_i^0	Baseline failure rate of root node B_i
$\mathcal{P}_i^B(t)/p_i^B(t)$	Prior failure probability of root node B_i at time t
$R_{\mathrm{FOWT}}(t)$	System reliability of the FOWT at time t
e	Observed abnormal evidence set
t_e	Occurrence time of a hazardous event
h	Specific hazard scenario (e.g. typhoon)
$\mathcal{D}_h$	Set of root-level nodes damaged by hazard scenario h
m_i^h	Hazard-induced failure acceleration multiplier for root node B_i
$\lambda_i^{\mathrm{deg}}(t)$	Effective failure rate of root node B_i during degradation stage
$p_i^{\mathrm{deg}}(t)$	Failure probability of root node B_i during degradation stage
$H_i^{\mathrm{deg}}(t)$	Cumulative hazard function during degradation stage
$\mathcal{P}_B^{\mathrm{deg}}(t)$	Degradation-stage root probability vector
$R_{\mathrm{FOWT}}^{\mathrm{deg}}(t)$	Degradation-stage reliability of the FOWT
$\Phi_{\mathrm{BN}}(\cdot)$	BN forward inference operator
$p_i^{\mathrm{base}}(t)$	Baseline failure probability of root node
$R_{\mathrm{FOWT}}^{\mathrm{base}}(t)$	Baseline reliability curve of the FOWT
$p_{\mathcal{B}}^{\mathrm{base}}(t)$	Baseline root-level failure probability vector
t_r	Repair start time
t_r^s	Under recovery strategy s
K	Repair budget (maximum number of repairable nodes)
s	Recovery strategy indicator
$\mathcal{R}_K^s$	Selected repair target set under strategy s and budget K
$\mathcal{C}_K^s$	Set of correctly repaired damaged roots
$\mathcal{M}_K^s$	Set of missed damaged roots
$\mathcal{W}_K^s$	Set of false repair targets
ρ_K^s	Damaged-root coverage ratio
$m_i^s(t)$	Recovered failure multiplier for root node B_i under strategy s
$\eta_i^s(t)$	Repair progress function
γ_s	Repair rate parameter for strategy s
m_i^{tar}	Target post-repair multiplier
m_s^{lim}	Repair limit multiplier
ξ_s	Residual repair-scar coefficient
$\lambda_i^s(t)$	Effective failure rate of root node B_i during recovery
$p_i^s(t)$	Root-level failure probability during recovery stage
$H_i^s(t)$	Cumulative hazard function during recovery stage

$\mathcal{P}_B^S(t)$	Recovery-stage root probability vector
$R_{\mathrm{FOWT}}^s(t)$	Reliability recovery trajectory under strategy s
K^*	Bounded target number
R_K^{BM}	Selected repair target set under Benchmark strategy
$\mathcal{C}_K^{\mathrm{BM}}$	Set of correctly repaired damaged roots under Benchmark strategy
t_r^{BM}	Benchmark repair start time
$\gamma_{\mathrm{BM}}/m_{\mathrm{BM}}^{\mathrm{lim}}/\xi_{\mathrm{BM}}$	Maintenance parameters for Benchmark strategy
$R_K^{\mathrm{OR}}/\mathcal{C}_K^{\mathrm{OR}}$	Target set/Correctly repaired set under Oracle strategy
$\mathcal{W}_K^{\mathrm{OR}}/\mathcal{M}_K^{\mathrm{OR}}$	False repair targets/Missed damaged roots under Oracle strategy
t_r^{phm}	Repair start time of the condition-aware strategy
Δt_{diag}	Additional diagnostic delay
α	Diagnostic accuracy
N_{phm}	Number of forward samples for condition-aware simulation
C_r	Number of correctly identified damaged roots in sample r
$\bar{R}_{\mathrm{FOWT}}^{\mathrm{phm}}(t)$	Ensemble mean recovery curve for condition-aware strategy
$\sigma_{\mathrm{phm}}(t)$	Sample standard deviation of the PHM recovery curves
T_1, T_2	Start and end times of resilience assessment window
t_k, t_{k+1}	Adjacent simulation discrete time points
$\mathrm{RI}_{\mathrm{phm}}$	Dynamic reliability index value under PHM strategy
$\mathrm{RI}_{\mathrm{BM}}$	Dynamic reliability index value under Benchmark strategy
$\Delta\mathrm{RI}$	Improvement of dynamic RI over the benchmark strategy

1. Introduction

1.1. Background

Renewable energy facilities are increasingly becoming an essential part of modern energy infrastructure, as many coastal regions and future low-carbon cities are expected to rely heavily on offshore wind power to achieve net-zero targets [1]. In this context, offshore wind energy assets should be considered alongside power grids and other energy systems as critical infrastructure because their failure may directly affect the continuity and security of renewable energy supply [2]. Traditionally, critical infrastructure has been expected to maintain high levels of reliability and safety during operation. However, under the increasing frequency and intensity of climate-induced extreme events, static reliability assessment alone is no longer sufficient to support infrastructure operation and recovery. Greater attention must be paid to the time-dependent evolution of system reliability before, during, and after disruptive events, particularly in terms of degradation propagation and recovery effectiveness [3]. This challenge is especially significant for FOWTs, which operate in harsh marine environments and are exposed to coupled wind–wave–current loading, limited maintenance accessibility, and prolonged post-disaster recovery periods [4]. Therefore, establishing a dynamic reliability assessment framework that captures both degradation and recovery processes is essential for supporting resilience improvement and ensuring the continuity, safety, and sustainability of renewable energy supply. Unlike conventional reliability assessment, which primarily focuses on failure probability during the service life, dynamic reliability assessment considers the temporal evolution of damage accumulation, functionality degradation, and post-event reliability restoration, thereby providing a quantitative basis for resilience-oriented decision-making and recovery planning [5].

To support resilience improvement throughout the lifecycle of FOWTs, system reliability should be analysed as an integral component of resilience, together with degradation and recovery processes. Therefore, understanding and quantifying the dynamic evolution of reliability during these processes is essential for overall resilience assessment [6]. The degradation process describes how system functionality deteriorates under disruptive events, whereas the recovery process characterizes how reliability and functionality are restored through maintenance, adaptation, and repair actions [7, 8]. Because resilience is closely related to the ability of a system to withstand degradation and recover from disruptions, various resilience-oriented assessment frameworks have been developed from perspectives such as vulnerability, robustness, rapidity, recoverability, maintainability, absorptive capacity, adaptive capacity, and restorative capacity [9]. These frameworks have been widely applied to transportation networks, power grids, communication systems, and other engineering infrastructure to evaluate system performance under disruption and recovery scenarios [10]. For example, previous studies have assessed infrastructure resilience through vulnerability analysis, recovery rapidity, data-driven modelling of weather-induced failures, and multi-dimensional performance indicators [11–14]. BNs and DBNs have also been increasingly adopted to model probabilistic dependencies, failure propagation mechanisms, and time-dependent degradation–recovery processes in complex engineering systems [15]. These developments provide valuable methodological foundations for dynamic reliability assessment and resilience-oriented decision-making.

1.2. State-of-the-art survey

1.2.1. Reliability degradation. Degradation assessment aims to characterize how offshore and marine assets progressively lose reliability, resistance, functionality, and operational performance under long-term deterioration processes and disruptive events. Existing studies have investigated degradation from both structural and system perspectives, demonstrating that reliability deterioration is driven by the combined effects of environmental loading, material degradation, uncertainty accumulation, and hazard-induced damage. At the structural level, considerable attention has been devoted to fatigue-induced degradation of offshore structures and critical components. Fatigue damage, fatigue life, and reliability

indices are commonly adopted to quantify the progressive deterioration of offshore wind turbine blade roots, tower structures, tubular members, and mooring systems subjected to wind, wave, current, and platform-motion loading [16]. To improve computational efficiency in fatigue assessment, surrogate modelling and active-learning-based approaches have been increasingly employed to estimate structural reliability under complex loading conditions [17, 18]. Beyond fatigue, corrosion-fatigue interaction has also been incorporated into degradation modelling, revealing that environmental deterioration can significantly reduce structural resistance and increase failure probability throughout the service life [19]. In addition to long-term deterioration, structural degradation is frequently assessed under extreme and accidental events. Earthquake loading, typhoon-wave hazards, and ship collisions have been widely investigated to evaluate structural response, damage severity, and safety margins [20–23]. In these studies, fragility, vulnerability, residual strength, ultimate limit state performance, reliability indices, and failure probabilities are commonly used to characterize the extent of structural deterioration and the likelihood of failure under uncertainty [24–26]. At the system level, degradation is increasingly understood as a process of functionality loss rather than merely the accumulation of component failures. Offshore wind farm studies have shown that turbine failures, collector-network disruptions, and subsystem interactions can collectively reduce system productivity, availability, and operational performance [27]. Other studies have highlighted the influence of downtime, maintenance accessibility, repair-resource limitations, weather windows, and energy production variability on overall system degradation [28]. Similar observations have been reported in port and maritime transportation systems, where local disruptions can propagate through interconnected infrastructures and generate cascading impacts on broader operational networks [29–32]. These studies demonstrate that system degradation emerges from the interaction between physical failures, operational constraints, and interdependent system behaviours. Methodologically, degradation assessment has evolved from traditional reliability analysis toward integrated approaches capable of representing both physical deterioration and system performance evolution. Reliability analysis, fragility assessment, and vulnerability analysis remain the primary tools for quantifying failure likelihood and damage severity. These methods are increasingly supported by finite element analysis, coupled aero-hydro-servo-elastic simulations, surrogate modelling, BNs, DBNs, Monte Carlo simulation, and network-based approaches to capture uncertainty propagation, failure evolution, and functionality loss across multiple scales.

Overall, existing degradation studies provide important foundations for understanding how offshore and marine assets lose reliability and functionality under deterioration and disruptive events. However, most studies focus either on component-level reliability deterioration or system-level performance degradation, with limited integration between physical degradation mechanisms and system-wide functionality evolution.

1.2.2. Reliability recovery. Recovery assessment focuses on the restoration of reliability, functionality, and operational performance following degradation or disruptive events. Compared with degradation assessment, recovery-oriented research remains relatively limited, although increasing attention has been given to performance restoration, maintenance planning, and resilience enhancement in offshore and marine systems. Existing studies commonly evaluate recovery using indicators such as repair time, recovery rate, restoration trajectory, reliability restoration, absorption capacity, and recovery capacity [33, 34]. At the structural level, recovery is primarily associated with inspection, maintenance, repair, and replacement activities aimed at restoring structural resistance and functionality after damage. Reliability-based inspection planning has been widely adopted to support maintenance decision-making and prevent progressive deterioration from developing into severe failures [35]. More recently, predictive maintenance frameworks have integrated structural condition monitoring, damage prediction, and maintenance optimization to improve recovery effectiveness and asset availability [36]. These developments indicate a gradual transition from reactive repair strategies toward proactive and condition-aware asset management. At the system level, recovery extends beyond physical restoration to encompass the recovery of operational continuity and service capability. Studies on offshore wind farms have shown that recovery performance is strongly influenced by maintenance logistics, vessel accessibility, spare-part availability, repair resources, and weather constraints [37]. Operational strategies such as coordinated dispatch and the integration of energy storage systems have further been shown to improve service continuity and mitigate disruption impacts following extreme events [38, 39]. In port and maritime transportation systems, recovery studies have emphasized the importance of managing interdependencies, uncertainty propagation, and adaptive decision-making throughout restoration processes [40, 41]. A variety of modelling approaches have been developed to support recovery assessment. DBNs, evidence theory, Monte Carlo simulation, scenario analysis, recovery trajectory modelling, and optimization-based approaches have been applied to represent restoration processes, uncertainty evolution, and resource-allocation decisions [13, 14, 42, 43]. Compared with conventional static reliability assessment, these methods provide improved capabilities for capturing the dynamic nature of post-disruption recovery and system adaptation.

Overall, existing recovery studies have expanded resilience assessment from structural repair toward broader evaluations of functionality restoration, operational continuity, and adaptive capacity. Nevertheless, degradation and recovery processes are still frequently modelled separately, while the interactions among degradation evolution, failure propagation, uncertainty updating, and recovery actions remain insufficiently represented. Consequently, there is a need for unified dynamic reliability frameworks capable of capturing the coupled evolution of degradation and recovery across both structural and system levels, thereby supporting resilience-oriented assessment and decision-making for offshore and marine assets.

Table 1. Comparison of existing studies and the proposed framework.

Framework capability	Degradation-oriented studies	Recovery-oriented studies	This study
Hazard-induced root-cause failure propagation	Partial	×	✓
Imperfect recovery and residual damage modelling	×	Partial	✓
PHM-informed recovery decision support	×	Partial	✓
Dynamic reliability assessment for resilience improvement	Partial	Partial	✓

1.3. Research gaps and contribution

As summarized in table 1, the existing literature still exposes several limitations.

First, although degradation-oriented and recovery-oriented studies have provided valuable insights into reliability deterioration and resilience restoration of offshore and marine systems, they are often investigated separately. Limited attention has been given to developing a unified framework capable of representing disaster-induced root-cause failure acceleration, failure propagation, imperfect recovery, and residual post-repair damage, and their combined influence on the dynamic reliability evolution of FOWT systems.

Second, although condition monitoring and PHM have been widely recognized as important tools for offshore wind operation and maintenance, their contribution to reliability recovery and resilience enhancement remains insufficiently quantified. In particular, the influence of root-cause failure identification accuracy on repair effectiveness, reliability restoration, and post-disaster resilience has not been systematically investigated.

To address these gaps, this study develops a BN-based dynamic reliability assessment framework for FOWT systems, in which disaster-induced root-cause failure acceleration, empirical maintenance-based recovery, and PHM-informed repair strategies are taken into account together. The main contributions of this study are summarized as follows:

1) A BN-based dynamic reliability assessment framework is developed to model disaster-induced reliability degradation of FOWT systems: The proposed framework represents the causal dependencies among root-cause failures, component failures, cascading effects, and system-level performance degradation. By accelerating multiple root-cause failure probabilities under disaster scenarios, the framework quantifies how external hazards affect the dynamic reliability evolution of the FOWT system. In addition, the recovery process is modelled by considering that conventional maintenance actions can only restore empirically identified root causes rather than the actual underlying root causes, thereby enabling the framework to capture imperfect recovery and residual post-repair reliability degradation.
2) A PHM-informed maintenance strategy is integrated to evaluate the influence of root-cause failure identification accuracy on system reliability recovery: The proposed framework simulates the capability of condition monitoring and PHM to inspect deeper root-cause failures and improve maintenance decision-making. By varying the fault-identification accuracy boundary of PHM-based maintenance, the study quantifies how PHM performance affects repair effectiveness, reliability restoration, and post-event resilience of the FOWT system. This contribution provides a dynamic reliability-based basis for evaluating the value of PHM in post-disaster recovery and resilience enhancement.

The remainder of this paper is organized as follows. Section 2 introduces the proposed dynamic reliability-based resilience assessment methodology. Section 3 presents a case study to demonstrate its application and effectiveness. Section 4 concludes the research.

2. Methodology

Dynamic reliability is defined in this study as the time-dependent evolution of system reliability during degradation and recovery processes following disruptive events. For FOWTs, hazardous events may trigger component failures, failure propagation, residual damage accumulation, and delayed recovery actions, all of which influence the overall reliability evolution of the system. In this section, a dynamic reliability assessment framework will be introduced for resilience enhancement for FOWTs.

2.1. Overall dynamic reliability assessment framework

A dynamic reliability perspective is required to evaluate how system performance deteriorates and is restored over time. As shown in figure 1, the framework provides a unified probabilistic structure to model failure dependencies, system-level reliability degradation, residual damage effects, and post-disruption recovery processes. The framework is intended to support resilience improvement by quantifying reliability deterioration and restoration under different maintenance and recovery strategies.

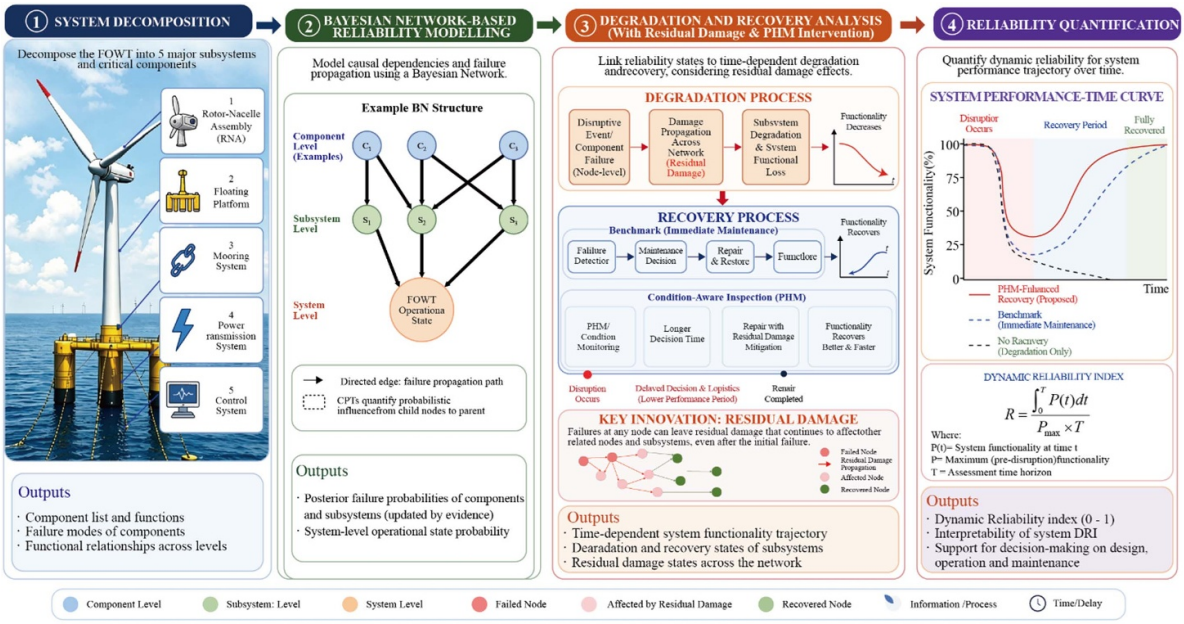


Figure 1. Overall framework for dynamic reliability assessment of FOWTs.

As shown in figure 1, the proposed dynamic reliability assessment framework for FOWTs consists of four main processes. Within the proposed framework, dynamic reliability assessment serves as the core analytical mechanism for quantifying the time-dependent evolution of system performance under degradation and recovery processes. Recovery represents the maintenance actions taken after disruptive events to restore system functionality, while condition-aware maintenance introduces PHM-enabled inspections to improve root-cause failure identification and repair effectiveness. By comparing the reliability restoration achieved under different recovery strategies, the framework evaluates their contributions to resilience enhancement. Therefore, resilience improvement is achieved through more effective recovery decisions, and dynamic reliability assessment provides the quantitative basis for measuring this improvement.

2.2. *Reliability model of FOWT system based on BN*

The hierarchical failure representation of the FOWT system based on literature [44] that provides a thorough physical configuration and functional failure propagation relationships on FOWTs.

As shown in figure 2, the FOWT is first decomposed into five major sub-systems. Each sub-system is further associated with a set of critical components or functional units, such as the mooring subsystem, tower, floating foundation, hydraulic subsystem, alarm facilities, lubrication system, gears, bearings, rotor and stator, wires, blades, and yaw subsystem.

Based on the system decomposition, figure 3 presents the corresponding BN for modelling failure propagation in FOWTs. The subsystem nodes S1–S5 represent the support structure, pitch system, gearbox, generator, and auxiliary system, respectively. Root causes, intermediate failure events, and subsystem failures are mapped into the BN according to the failure-event classification reported in literature [45]. Directed edges represent the causal dependencies among root failures, component failures, subsystem malfunctions, and the top event, namely FOWT malfunction. Through these probabilistic propagation paths, the BN captures how root-cause failures influence system-level functionality and reliability.

The BN is defined as a directed acyclic graph:

$$\mathcal{G} = (\mathcal{V}, \mathcal{E}) \tag{1}$$

where $\mathcal{V}$ is the set of nodes and $\mathcal{E}$ is the set of directed edges. The node set is defined as:

$$\mathcal{V} = \mathcal{B} \cup \mathcal{A} \cup \mathcal{S} \cup \{\mathcal{F}\} \tag{2}$$

where $\mathcal{B}$ is the set of root-level failure nodes, $\mathcal{A}$ denotes the set of observable abnormal nodes, $\mathcal{S}$ denotes the set of subsystem's nodes, and $\mathcal{F}$ denotes the top-level FOWT malfunction node. The directed edge set $\mathcal{E}$ represents causal failure propagation relationships from root-level causes to the overall FOWT malfunction state passing via observable abnormalities and subsystem states.

Let the root-level, observable abnormalities, and subsystem-level node sets be written as:

$$\begin{aligned} &\mathcal{B} = \{B_1, B_2, \ldots, B_{n_\mathcal{B}}\}, \\ &\mathcal{A} = \{A_1, A_2, \ldots, A_{n_\mathcal{A}}\}, \mathcal{S} = \{S_1, S_2, \ldots, S_{n_\mathcal{S}}\} \end{aligned} \tag{3}$$

where, and. Each node is modelled as a binary random variable:

$$B_i, A_j, S_k, F \in \{0,\ 1\}. \tag{4}$$

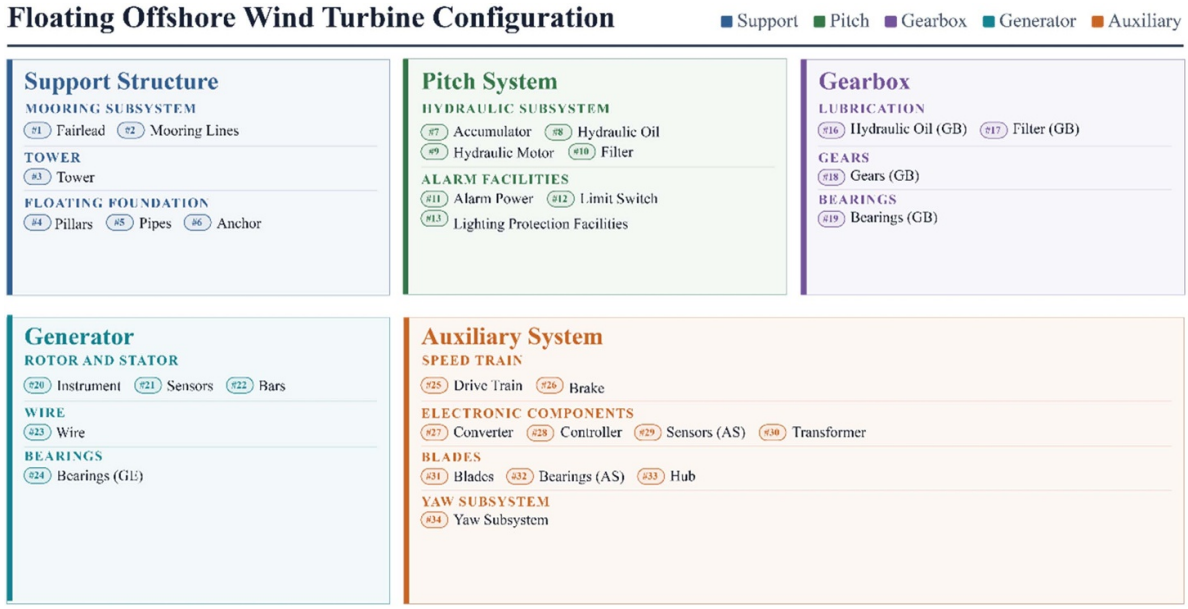


Figure 2. The configuration of the FOWT.

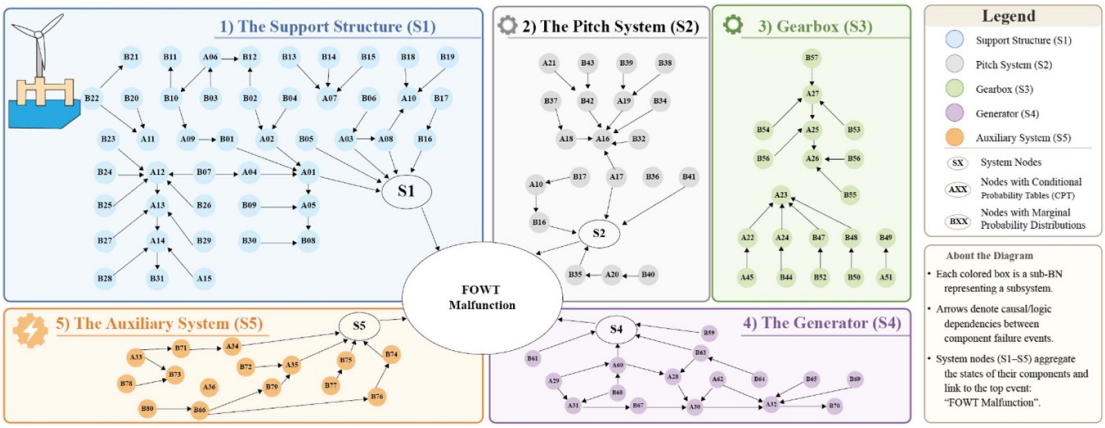


Figure 3. The BN model of FOWT.

The state value '0' denotes the normal state, while the state value '1' denotes the activated failure or abnormal state. Therefore, $B_i = 1$ indicates that the ith root-level failure mechanism or component-level failure mode has occurred, $A_j = 1$ indicates that the jth abnormal manifestation is present or observed, $S_k = 1$ indicates that the kth subsystem is failed or degraded, and $F = 1$ indicates the top-level FOWT malfunction.

Let denote the collection of random variables associated with all nodes in. According to the factorization property of BN, the joint probability distribution of can be expressed as:

$$P(\mathbb{X}_{\mathcal{V}}) = \prod_{X_l \in \mathcal{V}} P\left(X_l | \mathbb{X}_{\mathrm{pa}_{\mathcal{G}}(X_l)}\right) \tag{5}$$

where denotes an arbitrary node variable in the BN, denotes the parent-node set of in the directed graph. Is random variables associated with these parent nodes.

The BN used for FOWT system, the joint distribution can be written explicitly as:

$$P(\mathbb{X}_{\mathcal{V}}) = \prod_{i=1}^{n_{\mathcal{B}}} P(B_i) \prod_{j=1}^{n_{\mathcal{A}}} P\left(A_j | \mathbb{X}_{\mathrm{pa}_{\mathcal{G}}(A_j)}\right) \times \prod_{k=1}^{n_{\mathcal{S}}} P\left(S_k | \mathbb{X}_{\mathrm{pa}_{\mathcal{G}}(S_k)}\right) P\left(F | \mathbb{X}_{\mathrm{pa}_{\mathcal{G}}(F)}\right). \tag{6}$$

The root-level nodes are treated as prior failure nodes, while the observable abnormal nodes, subsystem-level nodes, and the top-level FOWT node are described by CPTs. For each root-level node B_i its binary state is governed by a time-dependent prior failure probability. The failure rate $\lambda_i(t)$ does not represent the node state directly; instead, it determines the probability that the corresponding root-level failure has occurred by time t:

$$\nu_i^B(t) = \mathcal{P}(B_i = 1; t). \tag{7}$$

Using the cumulative hazard formulation,

$$\mathcal{F}_i^B(t) = 1 - \mathrm{e}^{-\int_0^t \lambda_i(\tau)\mathrm{d}\tau}. \tag{8}$$

When the failure rate is constant over the considered time interval, this reduces to:

$$\mathcal{F}_i^B(t) = 1 - \mathrm{e}^{-\lambda_i \cdot t}. \tag{9}$$

Thus, the prior probability table of root node B_i at time t is:

$$P(B_i;t) = \left[P(B_i=0;t), P(B_i=1;t)\right] = \left[1-\mathcal{F}_i^B(t), \mathcal{F}_i^B(t)\right]. \tag{10}$$

For an observable abnormal node, the CPT describes the probability that the abnormal manifestation is activated under different parent root-node states:

$$P\left(A_j = 1 | \mathbb{X}_{\mathrm{pa}_\mathcal{G}(A_j)}\right). \tag{11}$$

The marginal abnormal probability of A_i at time t is obtained by summing over all parent-state configurations:

$$\begin{aligned} P(A_j=1;t) = &\sum_{\mathbb{X}_{\mathrm{pa}_\mathcal{G}(A_j)}} P\left(A_j=1|\mathbb{X}_{\mathrm{pa}_\mathcal{G}(A_j)} = \mathbb{X}_{\mathrm{pa}_\mathcal{G}(A_j)}\right) \\ &\times P\left(\mathbb{X}_{\mathrm{pa}_\mathcal{G}(A_j)} = \mathbb{X}_{\mathrm{pa}_\mathcal{G}(A_j)};t\right) \end{aligned} \tag{12}$$

where is a state configuration of the parent nodes of.

The same marginalisation procedure is then applied recursively to higher-level nodes. Specifically, the marginal probabilities of subsystem-level nodes are inferred from their parent observable abnormal nodes, and the top-level FOWT malfunction probability is inferred from its parent subsystem-level nodes. Therefore, the BN forward inference process can be compactly written as:

$$\begin{aligned} &\{P(B_i;t)\}_{i=1}^{n_\mathcal{B}} \\ &\quad \to \{P(A_j;t)\}_{j=1}^{n_\mathcal{A}} \to \{P(S_k;t)\}_{k=1}^{n_\mathcal{S}} \to P(F=1;t). \end{aligned} \tag{13}$$

The system reliability of the FOWT is defined as the probability that the top-level node remains in the normal state:

$$R_{\mathrm{FOWT}}(t) = P(F=0;t) = 1 - P(F=1;t). \tag{14}$$

For diagnostic inference, let the observed abnormal evidence be denoted by:

$$\mathrm{e} = \left\{A_{o_1}=1, A_{o_2}=1, \ldots, A_{o_q}=1\right\}, \left\{A_{o_1}, A_{o_2}, \ldots, A_{o_q}\right\} \subseteq \mathcal{A}. \tag{15}$$

Given, the posterior probability of each root-level node is estimated as:

$$P(B_i = 1 \mid e) = \frac{P(B_i=1, e)}{P(e)}. \tag{16}$$

The posterior probabilities are used as BN-based diagnostic weights for subsequent recovery-stage decision-making. Thus, the BN model provides two outputs for the subsequent resilience analysis: the forward-inferred FOWT reliability, and the posterior root-level diagnostic probabilities.

2.3. Degradation-stage modelling under hazardous events

The degradation stage describes how a hazardous event causes post-disaster performance loss of the FOWT. In this study, hazardous events are not imposed directly on the subsystem-level nodes or on the top-level FOWT node. Instead, the event is assumed to affect a subset of root-level failure nodes. These root-level nodes represent the underlying failure mechanisms or component-level failure modes that are physically aggravated by the disaster. The resulting changes in root-level failure probabilities are then propagated through the BN that has been introduced to update the top-level FOWT reliability. Let t_e denote the occurrence time of a hazardous event, and let h denote a specific hazard scenario, such as a typhoon or an earthquake. The set of root-level nodes damaged by hazard scenario h is defined as $\mathcal{D}_h \subseteq \mathcal{B}$, where $\mathcal{B}$ is the set of root-level failure nodes. A root node $B_i \in \mathcal{D}_h$ is regarded as a truly damaged root under the hazard scenario, while $B_i \notin \mathcal{D}_h$ is treated as not directly damaged by the event has taken place.

The main assumptions of the degradation-stage model are as follows. First, the hazardous event occurs at a specified time t_e, and it has no influence on the system before this time. Second, the direct physical impact of the hazard is represented at the root-node level by increasing the failure rates of selected damaged roots. Third, the damage state of the root nodes is not assumed to be directly observable. Instead, its effects are propagated through the BN and may appear as observable abnormal nodes. Fourth, without repair intervention, the hazard-induced failure acceleration remains active after the event.

For each root node B_i, a hazard-induced failure acceleration multiplier m_i^h is assigned. It is defined as:

$$m_i^h = \begin{cases} >1, & B_i \in \mathcal{D}_h, \\ 1, & B_i \notin \mathcal{D}_h. \end{cases} \tag{17}$$

Therefore, only the truly damaged roots experience an increase in their failure rates. For undamaged root nodes, the multiplier remains equal to one and the baseline failure process is unchanged.

Let λ_i^0 denote the baseline failure rate of root node B_i. During the degradation stage, the effective failure rate of B_i is defined as:

$$\lambda_i^{\mathrm{deg}}(t) = \begin{cases} \lambda_i^0, & t < t_e, \\ \lambda_i^0 m_i^h, & t \geqslant t_e. \end{cases} \tag{18}$$

This event-based formulation ensures that the disaster does not affect the system before its occurrence time. After the event, damaged root nodes experience accelerated failure, while undamaged root nodes continue to follow their baseline failure rates.

The corresponding failure probability of root node B_i under the degradation stage is calculated using the cumulative hazard function:

$$\mathcal{F}_i^{\mathrm{deg}}(t) = \mathcal{F}(B_i=1;t,h) = 1 - \mathrm{e}^{-H_i^{\mathrm{deg}}(t)} \tag{19}$$

where $H_i^{\deg}(t) = \int_0^t \lambda_i^{\deg}(\tau)\,\mathrm{d}\tau$. Substituting the event-based effective failure rate gives:

$$\mathscr{P}_i^{\deg}(t) = \begin{cases} 1 - \mathrm{e}^{-\lambda_i^0 t}, & t < t_e, \\ 1 - \mathrm{e}^{-\lambda_i^0 t_e - \lambda_i^{\deg}(t-t_e)}, & t \geq t_e. \end{cases} \quad (20)$$

This expression indicates that before the disaster, the root node follows its baseline degradation process. After the disaster, the accumulated failure risk consists of two parts: the baseline risk accumulated before the event and the accelerated risk accumulated after the event. The degradation-stage root probability vector for all $n_B = \mid B \mid$ root-level failure nodes is then defined as:

$$\mathscr{P}_{\mathcal{B}}^{\deg}(t) = \left[\mathscr{P}_1^{\deg}(t), \mathscr{P}_2^{\deg}(t), \ldots, \mathscr{P}_{n_B}^{\deg}(t)\right]. \quad (21)$$

This vector represents the updated prior failure probabilities of all root-level nodes after considering the hazardous event. It is then assigned to the root-level nodes of the BN.

Using the BN forward inference process defined in the previous section, the updated root-level probabilities are propagated to observable abnormal nodes, subsystem-level nodes, and finally to the top-level FOWT malfunction node. The degradation-stage reliability of the FOWT is therefore obtained as:

$$R_{\mathrm{FOWT}}^{\deg}(t) = P(F=0;t,h) = 1 - P(F=1;t,h). \quad (22)$$

Equivalently, the degradation-stage reliability can be written as a BN inference mapping:

$$R_{\mathrm{FOWT}}^{\deg}(t) = \Phi_{\mathrm{BN}}\left(\mathscr{P}_{\mathcal{B}}^{\deg}(t)\right) \quad (23)$$

where $\Phi_{\mathrm{BN}}(\cdot)$ denotes the BN forward inference operator from root-level failure probabilities to top-level FOWT reliability. For comparison, the baseline case without disaster impact is obtained by setting all hazard multipliers equal to one:

$$m_i^h = 1, \forall B_i \in \mathcal{B}. \quad (24)$$

The baseline root-level failure probability is therefore:

$$\mathscr{P}_i^{\mathrm{base}}(t) = 1 - \mathrm{e}^{-\lambda_i^0 t}. \quad (25)$$

The baseline reliability curve is:

$$R_{\mathrm{FOWT}}^{\mathrm{base}}(t) = \Phi_{\mathrm{BN}}\left(p_{\mathcal{B}}^{\mathrm{base}}(t)\right) \quad (26)$$

where $\mathscr{P}_{\mathcal{B}}^{\mathrm{base}}(t) = \left[\mathscr{P}_1^{\mathrm{base}}(t), \mathscr{P}_2^{\mathrm{base}}(t), \ldots, p_{n_B}^{\mathrm{base}}(t)\right]$.

The difference between $R_{\mathrm{FOWT}}^{\mathrm{base}}(t)$ and $R_{\mathrm{FOWT}}^{\deg}(t)$ represents the reliability loss caused by the hazardous event. The curve $R_{\mathrm{FOWT}}^{\deg}(t)$ is also referred to as the hazard-only degradation trajectory, because it describes the post-disaster reliability evolution before any repair action is applied. This degradation trajectory provides the initial post-disaster performance loss for the subsequent recovery-stage modelling.

2.4. Recovery modelling by maintenance

The recovery stage describes how repair actions are applied after the hazardous event and how the degraded FOWT reliability is restored over time. In this study, recovery is modelled at the root-node level. This is consistent with the degradation-stage model, where the hazardous event directly increases the failure risks of selected root-level failure nodes. Therefore, maintenance actions are also represented by reducing the hazard-induced failure acceleration of repaired root nodes.

Let t_r denote start time to repair. For a damaged root node $B_i \in \mathcal{D}_h$, repair can reduce its hazard-induced multiplier only if this root is correctly selected as a repair target. For root nodes that are not selected for repair, or for false repair targets that are not truly damaged, no improvement is made to the truly damaged roots. This assumption allows the model to explicitly represent the effect of diagnostic errors and limited repair resources.

Let K denote the repair budget, namely the maximum number of root-level nodes that can be repaired. For a given recovery strategy s, the selected repair target set is denoted by:

$$\mathcal{R}_K^s \subseteq \mathcal{B}, |R_K^s| \leqslant K \quad (27)$$

where s can represent the benchmark strategy, the condition-aware strategy, or the oracle strategy. The set of correctly repaired damaged roots is:

$$\mathcal{C}_K^s = \mathcal{R}_K^s \cap \mathcal{D}_h. \quad (28)$$

Only nodes in $\mathcal{C}_K^s$ contribute to reliability recovery. The missing damaged roots are:

$$\mathcal{M}_K^s = \mathcal{D}_h \setminus \mathcal{R}_K^s \quad (29)$$

and the false repair targets are:

$$\mathcal{W}_K^s = \mathcal{R}_K^s \setminus \mathcal{D}_h. \quad (30)$$

The repair effectiveness can therefore be described by the damaged-root coverage ratio:

$$\rho_K^s = \frac{\mid \mathcal{C}_K^s \mid}{\mid \mathcal{D}_h \mid}, \mid \mathcal{D}_h \mid > 0. \quad (31)$$

A higher coverage ratio indicates that more truly damaged roots are correctly repaired under the available repair budget. For each correctly repaired damaged root $B_i \in \mathcal{C}_K^s$, the hazard-induced failure acceleration is gradually reduced after the repair starts. Since m_i^h represents the hazard-induced multiplier before repair, the recovered multiplier under strategy s is defined as:

$$m_i^s(t) = m_i^h - \eta_i^s(t)\left(m_i^h m_i^{\mathrm{tar}}\right), t \geqslant t_r^s \quad (32)$$

where t_r^s is the repair start time of strategy s, and $\eta_i^s(t)$ is the repair progress function. In this study, the repair progress is modelled as:

$$\eta_i^s(t) = 1 - \mathrm{e}^{-\gamma_s(t-t_r^s)}, t \geqslant t_r^s \quad (33)$$

where γ_s is the repair rate parameter. A larger γ_s indicates a faster recovery process after repair begins. The target post-repair multiplier is defined as:

$$m_i^{\mathrm{tar}} = \max\left(m_s^{\mathrm{lim}}, 1 + \left(m_i^h - 1\right)\xi_s\right) \tag{34}$$

where m_s^{lim} is the repair limit multiplier and ξ_s is the residual repair-scar coefficient. The repair limit multiplier controls the minimum achievable failure multiplier after repair, while the repair-scar coefficient represents residual damage that cannot be completely removed by maintenance. If $\xi_s = 0$ and $m_s^{\mathrm{lim}} = 1$, the repaired root can theoretically return to its baseline failure multiplier. If $\xi_s > 0$, part of the hazard-induced damage remains after repair. For $t < t_r^s$, no repair effect is applied and the multiplier remains $m_i^s(t) = m_i^h$.

For damaged roots that are not correctly repaired, the multiplier remains at its hazard-induced level:

$$m_i^s(t) = m_i^h, B_i \in \mathcal{D}_h \setminus \mathcal{C}_K^s. \tag{35}$$

For undamaged roots, the multiplier remains equal to one unless they are selected as false repair targets. Since false repair targets do not correspond to true damaged roots, they consume repair resources but do not reduce the risk of the actual damaged root set. The effective failure rate of root node B_i during recovery is therefore expressed as:

$$\lambda_i^s(t) = \lambda_i^0 m_i^s(t). \tag{36}$$

The corresponding root-level failure probability is calculated through the cumulative hazard function:

$$\mathcal{F}_i^s(t) = 1 - \mathrm{e}^{-H_i^s(t)} \tag{37}$$

where $H_i^s(t) = \int_0^t \lambda_i^s(\tau)\,\mathrm{d}\tau$ The recovery-stage root probability vector is then given below:

$$\mathcal{F}_{\mathcal{B}}^s(t) = \left[\mathcal{F}_1^s(t), \mathcal{F}_2^s(t), \ldots, \mathcal{F}_{n_B}^s(t)\right]. \tag{38}$$

Using the BN forward inference operator, the reliability recovery trajectory under strategy s is obtained as:

$$R_{\mathrm{FOWT}}^s(t) = \Phi_{\mathrm{BN}}\left(\mathcal{F}_{\mathcal{B}}^s(t)\right). \tag{39}$$

This reliability trajectory describes how the FOWT system recovers over time after repair actions are applied. The benchmark recovery strategy represents conventional experience-based repair decision-making using observable post-disaster symptoms and BN posterior diagnostic information. In practice, conventional recovery often relies on observed abnormal manifestations, engineering experience, and limited monitoring information. In this study, this process is represented by using the BN-based posterior diagnostic weights obtained from the observed abnormal A-nodes. Given the observed abnormal evidence e, the posterior probability: $P(B_i = 1 \mid e)$, which indicates the likelihood that root node B_i is responsible for the observed abnormal manifestations. The benchmark strategy selects the repair target set by maximizing the total BN posterior diagnostic probability under the repair budget K:

$$\mathcal{R}_K^{\mathrm{BM}} = \arg\max_{\mathcal{R}\in\mathcal{B}} \sum_{B_i\in\mathcal{R}} P(B_i = 1|e). \tag{40}$$

This means that the K root nodes with the largest BN posterior diagnostic weights are selected for repair. Since the true damaged root set $\mathcal{D}_h$ is not directly observable, the benchmark strategy may repair some wrong roots and miss some true damaged roots. Its correctly repaired root set is:

$$\mathcal{C}_K^{\mathrm{BM}} = \mathcal{R}_K^{\mathrm{BM}} \cap \mathcal{D}_h. \tag{41}$$

The benchmark repair start time is denoted by t_r^{BM}. The benchmark repair process is controlled by the repair rate γ_{BM}, repair limit multiplier $m_{\mathrm{BM}}^{\mathrm{lim}}$, and residual repair-scar coefficient ξ_{BM}. These parameters determine how quickly and how completely the correctly repaired damaged roots can recover.

There is an oracle recovery strategy introduced as an idealized upper-bound reference. Unlike the benchmark strategy, the oracle strategy assumes perfect knowledge of the true damaged root set $\mathcal{D}_h$. This represents a hypothetical situation in which the post-disaster inspection can identify the true damaged roots with perfect accuracy. However, the Oracle strategy is still constrained by the same repair budget K. If the number of true damaged roots exceeds the repair budget, only part of $\mathcal{D}_h$ can be repaired.

The Oracle strategy selects the $K^* = \min(K, |\mathcal{D}_h|)$ truly damaged roots with the largest hazard-induced failure acceleration multipliers. Mathematically, the Oracle repair target set is:

$$\mathcal{R}_K^{\mathrm{OR}} = \arg\max_{\mathcal{R}\in\mathcal{D}_h, |\mathcal{R}|=K^*} \sum_{B_i\in\mathcal{R}} m_i^h. \tag{42}$$

This means that the oracle strategy prioritizes the most severely affected damaged roots. Since the selected roots are always drawn from $\mathcal{D}_h$, the Oracle strategy has no false repair targets:

$$\mathcal{W}_K^{\mathrm{OR}} = \mathcal{R}_K^{\mathrm{OR}} \setminus \mathcal{D}_h = \emptyset. \tag{43}$$

Its correctly repaired damaged-root set is:

$$\mathcal{C}_K^{\mathrm{OR}} = \mathcal{R}_K^{\mathrm{OR}} \cap \mathcal{D}_h = \mathcal{R}_K^{\mathrm{OR}}. \tag{44}$$

The missed damaged-root set is:

$$\mathcal{M}_K^{\mathrm{OR}} = \mathcal{D}_h \setminus \mathcal{R}_K^{\mathrm{OR}}. \tag{45}$$

The oracle strategy is not intended to represent a practical inspection method. Instead, it provides a theoretical upper-bound reference for evaluating the performance loss caused by imperfect diagnosis and limited observability.

The condition-aware recovery strategy represents a PHM-informed repair decision-making approach, where repair targets are selected based on deep inspection and condition

assessment. Compared with the benchmark strategy, it incorporates additional condition information and diagnostic capability. However, this improved diagnosis may require additional time before repair actions can begin. The condition-aware repair start time is defined as:

$$t_r^{\mathrm{phm}} = t_r^{\mathrm{BM}} + \Delta t_{\mathrm{diag}} \tag{46}$$

where Δt_{diag} is the additional diagnostic delay. A larger Δt_{diag} means that repair starts later, allowing the degraded system to continue accumulating failure risk before recovery begins. The diagnostic accuracy of the condition-aware strategy is denoted by $\alpha \in [0,1]$.

This parameter represents the probability that a selected repair target is a truly damaged root. When $\alpha = 1$, the condition-aware strategy perfectly identifies damaged roots under the repair budget. When $\alpha < 1$, the repair target set may include false repair targets. To represent diagnostic uncertainty, the condition-aware repair decision is simulated using N_{phm} forward samples. For the rth sample, the repair target set is:

$$\mathcal{R}_{K,r}^{\mathrm{phm}}, r = 1,2,\ldots,N_{\mathrm{phm}}. \tag{47}$$

The correctly repaired damaged-root set is

$$\mathcal{C}_{K,r}^{\mathrm{phm}} = \mathcal{R}_{K,r}^{\mathrm{phm}} \cap \mathcal{D}_h. \tag{48}$$

Let $C_r = \left| \mathcal{C}_{K,r}^{\mathrm{phm}} \right|$ denote the number of correctly identified damaged roots in sample r. Under diagnostic accuracy α, C_r is modelled as: $C_r \sim \mathrm{Binomial}(K^*, \alpha)$, where $K^* = \min(K, |\mathcal{D}_h|)$. The sampled value is bounded by $0 \leqslant C_r \leqslant K^*$. For sample r, C_r repair targets are selected from the true damaged set $\mathcal{D}_h$, while the remaining $K - C_r$ targets are selected from the non-damaged candidate set. Thus, $\mathcal{R}_{K,r}^{\mathrm{phm}} = \mathcal{C}_{K,r}^{\mathrm{phm}} \cup \mathcal{W}_{K,r}^{\mathrm{phm}}$, where $\mathcal{C}_{K,r}^{\mathrm{phm}} \subseteq \mathcal{D}_h$, and $\mathcal{W}_{K,r}^{\mathrm{phm}} \subseteq \mathcal{B} \setminus \mathcal{D}_h$.

The false repair target set $\mathcal{W}_{K,r}^{\mathrm{phm}}$ represents repair actions caused by diagnostic uncertainty. These targets consume repair resources but do not contribute to the recovery of truly damaged roots. For each PHM forward sample r, a recovery reliability curve is generated as:

$$R_{\mathrm{FOWT},r}^{\mathrm{phm}}(t) = \Phi_{\mathrm{BN}}\left(\mathcal{B}_{,r}^{\mathrm{phm}}(t)\right). \tag{49}$$

The ensemble mean recovery curve is:

$$\bar{R}_{\mathrm{FOWT}}^{\mathrm{phm}}(t) = \frac{1}{N_{\mathrm{phm}}} \sum_{r=1}^{N_{\mathrm{phm}}} R_{\mathrm{FOWT},r}^{\mathrm{phm}}(t). \tag{50}$$

The sample standard deviation is:

$$\sigma_{\mathrm{phm}}(t) = \sqrt{\frac{1}{N_{\mathrm{CA}} - 1} \sum_{r=1}^{N_{\mathrm{CA}}} \left(R_{\mathrm{FOWT},r}^{\mathrm{phm}}(t) - \bar{R}_{\mathrm{FOWT}}^{\mathrm{phm}}(t) \right)^2}. \tag{51}$$

This ensemble formulation allows the condition-aware strategy to represent both the expected recovery trajectory and the uncertainty caused by imperfect diagnosis.

The condition-aware strategy, known as PHM, is controlled by the repair budget K, diagnostic accuracy α, diagnostic delay Δt_{diag}, number of deep inspection forward samples N_{phm}, repair rate γ_{phm}, repair limit multiplier $m_{\mathrm{phm}}^{\mathrm{lim}}$, and residual repair-scar coefficient ξ_{phm}.

2.5. Dynamics reliability quantification

In this study, the dynamic reliability performance of the FOWT is quantified using the time-dependent system reliability trajectory during the post-disaster degradation and recovery process. The system reliability $R(t)$ is obtained from the BN-based reliability model at each simulation time step. A higher value of $R(t)$ indicates a higher probability that the FOWT remains in its normal operational state. Therefore, the reliability-time trajectory is used to characterize the evolution of system reliability throughout degradation and recovery, the dynamic RI is defined as:

$$\mathrm{RI} = \frac{1}{T_2 - T_1} \int_{T_1}^{T_2} \mathrm{R}(t)\,\mathrm{d}t \tag{52}$$

where T_1 and T_2 are the start and end times of the resilience assessment window, respectively. In this study, T_1 is set as the disaster event time and T_2 represents the end of the simulation period. The RI therefore represents the average retained reliability of the FOWT throughout the degradation and recovery processes.

Since the simulation is conducted at discrete time steps, the RI is calculated numerically as:

$$\mathrm{RI} = \frac{1}{T_2 - T_1} \sum_{k=1}^{N-1} \frac{R(t_k) + R(t_{k+1})}{2} (t_{k+1} - t_k) \tag{53}$$

where t_k and t_{k+1} are two adjacent simulation time points within the assessment window. This trapezoidal approximation is consistent with the reliability curve generated in the simulation.

Several RI values are calculated for comparison. The baseline RI represents the reference case without disaster-induced damage. The hazard-only RI represents the reliability evolution of the damaged system without repair intervention. The benchmark RI represents the recovery performance achieved using BN-posterior-based repair target selection. The condition-aware RI represents the reliability restoration achieved using condition-aware diagnosis and repair. For condition-aware recovery, multiple forward simulations are conducted to account for diagnostic uncertainty. Consequently, mean, lower-percentile, and upper-percentile reliability trajectories are used to calculate the corresponding mean, lower-bound, and upper-bound RI values.

To evaluate the benefit of condition-aware recovery, the improvement over the benchmark strategy is defined as:

$$\Delta RI = \mathrm{RI}_{\mathrm{phm}} - \mathrm{RI}_{\mathrm{BM}} \tag{54}$$

where $\mathrm{RI}_{\mathrm{phm}}$ and $\mathrm{RI}_{\mathrm{BM}}$ denote the dynamic RI values of the condition-aware and benchmark recovery strategies, respectively. A positive ΔRI indicates that condition-aware diagnosis improves reliability restoration compared with the benchmark strategy, whereas a negative value indicates that the benefit of improved diagnosis is insufficient to compensate for diagnostic delay or repair-resource limitations.

The dynamic RI converts each reliability trajectory into a scalar performance indicator, enabling direct comparison among different recovery strategies, repair budgets, diagnosis accuracies, and diagnostic delays. In this way, both the temporal reliability restoration process and the overall post-disaster dynamic reliability performance of the FOWT can be systematically evaluated. The resulting reliability-based metrics further provide quantitative support for resilience improvement and recovery decision-making.

3. Case study

3.1. Hazard-induced degradation simulation case definition for the FOWT system

There is a case study constructing a representative post-disaster degradation and recovery scenario for the FOWT system. Taking a typhoon as an example of a natural hazard frequently encountered by offshore wind systems, the affected root causes are selected to represent failure mechanisms in disaster-sensitive FOWT subsystems. This selection is literature-informed rather than arbitrary. Previous studies have shown that typhoon conditions can threaten the stability and structural integrity of offshore wind turbines and may cause severe blade damage, tower collapse, foundation overturning, and other structural failures under extreme wind speed, rapid wind-direction changes, turbulence, and coupled wind–wave loading [46]. For FOWTs, failure analysis studies further indicate that vulnerable subassemblies include the floating platform, mooring lines, tower structure, pitch and hydraulic system, blade control system, gearbox, generator, and other mechanical, electrical, and structural components [47, 48]. Therefore, the selected affected roots in table 2 are used to represent root-cause failure mechanisms distributed across these disaster-sensitive subsystems.

Following common practice in reliability engineering, hazardous-event effects are represented by failure-rate acceleration multipliers applied to baseline component failure rates [50]. The multipliers are assigned according to the relative exposure and vulnerability of selected root-cause mechanisms to extreme wind, rapid wind-direction changes, turbulence, and coupled platform–mooring–turbine loading [51, 52]. More directly exposed roots are assigned larger multipliers, while indirectly affected roots are assigned smaller ones. Therefore, the values in table 1 are interpreted as scenario-based relative degradation factors rather than exact empirical failure rates, and their influence is further examined through sensitivity analysis.

Table 2. Definition of the hazard-induced root damage scenario [49].

Damage severity level	Affected root nodes	Failure-rate acceleration multiplier
Very high	B13, B10, B12	4.5∼5.0
High	B27, B29, B30	3.2∼3.8
Medium-high	B31, B06, B78, B28, B79, B80	2.3∼2.8
Medium	B07, B08, B09, B11, B14, B22, B23, B25, B26	2.0∼2.2
Low-medium	B15, B16, B20, B24, B21	1.7∼1.8
Low	B47, B64, B71, B76	1.5∼1.6

3.2. Recovery simulation and definition of maintenance strategies

The post-disaster recovery scenario is established to evaluate how different diagnosis and repair strategies restore the reliability of the FOWT system. Three recovery strategies are considered: benchmark recovery, condition-aware inspection recovery, and oracle recovery. The benchmark recovery strategy is formulated as a Bayesian diagnosis-driven repair process. BNs are suitable for this task because they can encode probabilistic dependencies between observable symptoms and latent failure causes and update the likelihood of candidate causes when new evidence becomes available [53]. In wind turbine applications, BN-based diagnostic models have been used to infer failure root causes from SCADA- or monitoring-based symptoms, while offshore wind maintenance studies have used Bayesian updating to support inspection and repair decisions under uncertainty. Therefore, in this study, the abnormal post-disaster observable manifestations are used as diagnostic evidence to compute BN-posterior diagnosis weights for candidate roots, and the benchmark strategy selects the highest-ranked roots for repair under each repair budget [54].

The condition-aware inspection recovery strategy represents a state-aware recovery process supported by additional condition information [55]. Unlike the benchmark strategy, which uses a deterministic BN-posterior ranking, the condition-aware inspection strategy considers diagnostic accuracy, diagnostic delay, and uncertainty in the identified damaged roots [56]. This design is consistent with offshore wind condition-based maintenance studies, where condition monitoring, fault diagnosis, prognosis, and maintenance optimisation are integrated to support maintenance planning. It is also consistent with DBN-based wind turbine diagnostics and prognostics, where degradation information and future failure behaviour are explicitly modelled under uncertainty [57].

The oracle recovery strategy, also referred to here as the ideal reference strategy, assumes that the truly affected roots

Table 3. Post-disaster damage observations and diagnostic evidence.

Item	Definition in this case study
Truly affected roots	B13, B10, B12, B27, B29, B30, B31, B06, B78, B28, B79, B80, B07, B08, B09, B11, B14, B22, B23, B25, B26, B15, B16, B24, B20, B21, B47, B64, B71, B76
Abnormal observable manifestations	A01, A05, A02, A06, A12, A13, A34, A35, A16, A15
Benchmark diagnostic basis	Uses abnormal observable manifestations as BN evidence and ranks candidate roots according to posterior diagnosis weights
Condition-aware inspection basis	Uses abnormal observable manifestations together with additional state-aware diagnostic information, diagnostic accuracy, diagnostic delay, and uncertainty
Oracle information basis	Assumes perfect knowledge of the truly affected roots

Table 4. Summary of benchmark repair outcomes under different repair budgets.

Repair budget (No. of failed roots)	Correct repairs	Missed roots	Wrong repairs	Coverage
12	12	18	0	0.40
15	13	17	2	0.43
18	13	17	5	0.43
21	16	14	5	0.53
24	19	11	5	0.63
27	22	8	5	0.73
30	23	7	7	0.77

are perfectly known and repaired with priority under the same repair budget [58]. It does not represent a practical maintenance process, because real post-disaster diagnosis is affected by incomplete observations, imperfect sensing, and delayed inspection [59]. Instead, the oracle strategy provides an upper-bound reference for separating the effect of limited repair resources from the effect of imperfect damage identification. This is consistent with resilience-oriented post-disaster recovery studies, where recovery is commonly formulated as a repair-scheduling or resource-allocation problem under limited repair resources [60].

In the defined degradation scenario, the hazardous event affects a set of root-cause nodes. Through BN propagation, these root-level degradations generate abnormal observable manifestations at the observation layer. These abnormal manifestations are used as diagnostic evidence for both the benchmark recovery and condition-aware inspection recovery strategies. The relationship between true root damage, observable manifestations, and the diagnostic basis for each strategy is summarized in table 3.

To examine the influence of repair resources, multiple repair budgets are considered to represent different levels of post-disaster maintenance capacity. For each budget, the benchmark strategy selects repair targets according to the BN-posterior diagnosis ranking. The selected targets are then compared with the truly affected roots to identify correct repairs, missed affected roots, wrong repair targets, and coverage. The detailed benchmark repair outcomes are summarized in table 4 to support transparency and reproducibility. As shown in table 3, increasing the repair budget does not necessarily lead to a proportional increase in the coverage of truly affected roots. This is because some additional repair actions may be assigned to roots that are highly ranked by the BN diagnosis but are not truly affected. Therefore, benchmark recovery performance is determined not only by available repair resources, but also by the quality of the BN-based diagnostic ranking.

For the benchmark strategy, repair targets are selected based on the posterior diagnostic probabilities obtained from the BN. Specifically, once abnormal subsystem states are observed, the BN updates the likelihood of each candidate root cause by combining the observed malfunction evidence with prior expert knowledge embedded in the network structure and CPTs. The root nodes are then ranked according to their posterior probabilities, and the highest-ranked roots are selected as benchmark repair targets. For reproducibility, the complete benchmark repair target sets are reported in the appendix.

For the condition-aware inspection strategy, the same repair budgets are used to ensure a consistent comparison with the benchmark strategy, while the detailed design settings are summarized in table 5. In addition, two condition-information-related factors are considered: diagnosis delay and diagnosis accuracy. For each combination of repair budget, diagnosis delay, and diagnosis accuracy, multiple diagnostic samples are generated to represent uncertainty in root-cause identification. Therefore, the condition-aware inspection strategy does not correspond to a single deterministic repair target set. Instead, each sampled repair target set may contain correctly identified affected roots and incorrectly identified roots. The resulting recovery trajectories are summarized using the mean response and percentile bounds. This allows the recovery analysis to reflect both the benefit of improved state-aware inspection information and the uncertainty caused by delayed or imperfect diagnosis.

Since the simulation-based resilience framework developed for FOWTs depends on the repair-rate parameter γ_s, which governs the recovery speed of the repair strategy, and the failure-acceleration multiplier m_i^h, which amplifies the root failure rate under hazardous events, a sensitivity analysis was performed for these two parameters, and their impacts on the RI are discussed in the following section 3.8. The simulation setting is shown in table 6.

Table 5. Condition-aware inspection (PHM) recovery design.

Item	Setting
Repair budgets	Same budget levels as benchmark recovery
Diagnosis delay	0, 10, 20, 40, and 50 h
Diagnosis accuracy	0.55, 0.65, 0.75, 0.85 and 0.95
Repair target property	Non-deterministic; multiple possible repair target sets are generated under diagnostic uncertainty
Recovery output	Mean recovery trajectory, lower percentile trajectory, upper percentile trajectory, and corresponding resilience index values
Comparison basis	Compared with benchmark recovery under the same repair budget and with oracle recovery as the upper-bound reference

Note: The global simulation horizon was set to $\boldsymbol{T_{total}} = 1000$ h, with the hazard event occurring at $\boldsymbol{t_e} = 50$ h. The benchmark recovery strategy was initiated at $\boldsymbol{t_r^{BM}} = 200$ h under the same repair budget as the condition-aware strategy. The repair process was characterised by three common parameters: the repair rate parameter $\gamma_s = 0.50$, The hazard-induced failure acceleration multiplier $\boldsymbol{m_i^h}$ was scaled by an amplification factor as 1.0 in this study.

Table 6. Sensitivity-analysis design for repair-rate and hazard-induced failure acceleration parameters.

Item	Setting
repair-rate: γ_s	0.5∼0.8
Hazard Intensity Scale: $\boldsymbol{m_i^h}$	0.5∼1.5

Note: In this sensitivity study, only the repair-rate parameter γ_s and the hazard IntensityScale were varied, while all other model settings were fixed at their baseline values. The global simulation horizon was set to $\boldsymbol{T_{total}} = 1000$ h, with the hazard event occurring at $\boldsymbol{t_e} = 50$ h. For the benchmark strategy, the repair budget was fixed at 12, the diagnosis-weight mode was set to posterior, the repair-limit multiplier was 1.0, the benchmark repair started at $\boldsymbol{t_r^{BM}} = 200$ h. For the condition-aware strategy (PHM), the diagnosis accuracy was fixed at 0.80, the repair budget was 12, and the PHM repair started with a delay of 50 h after the benchmark repair.

Overall, the recovery scenario is designed to be interpretable and reproducible. The benchmark strategy evaluates recovery based on BN-posterior diagnosis using only abnormal observable manifestations. The condition-aware inspection strategy evaluates recovery when additional state-aware information is available but uncertain. The oracle strategy provides the ideal upper-bound recovery performance under the same repair budget. By comparing these three strategies, the study quantifies how repair resources, diagnostic quality, diagnostic delay, and uncertainty in root-cause identification influence the post-disaster recovery trajectory and dynamic RI.

4. Discussion and analysis

4.1. Overall performance comparison

Figure 4(a) shows the post-disaster reliability trajectories under different recovery strategies. Following the hazardous event, system reliability decreases significantly due to disaster-induced root-level failures. All recovery strategies improve the reliability trajectory relative to the hazard-only case. Among them, the benchmark strategy provides partial recovery, the condition-aware strategy achieves greater reliability restoration, and the oracle strategy serves as the ideal upper-bound reference.

Figure 4(b) compares the corresponding DRI values. Consistent with the reliability trajectories, the hazard-only case yields the lowest DRI, while the benchmark, condition-aware, and oracle strategies achieve progressively higher DRI values. Overall, the results indicate that improved fault diagnosis enhances recovery effectiveness and post-disaster reliability restoration. The sensitivity of this improvement to diagnostic performance is examined in the following section.is.

4.2. Sensitivity to PHM accuracy, delay, and repair budget

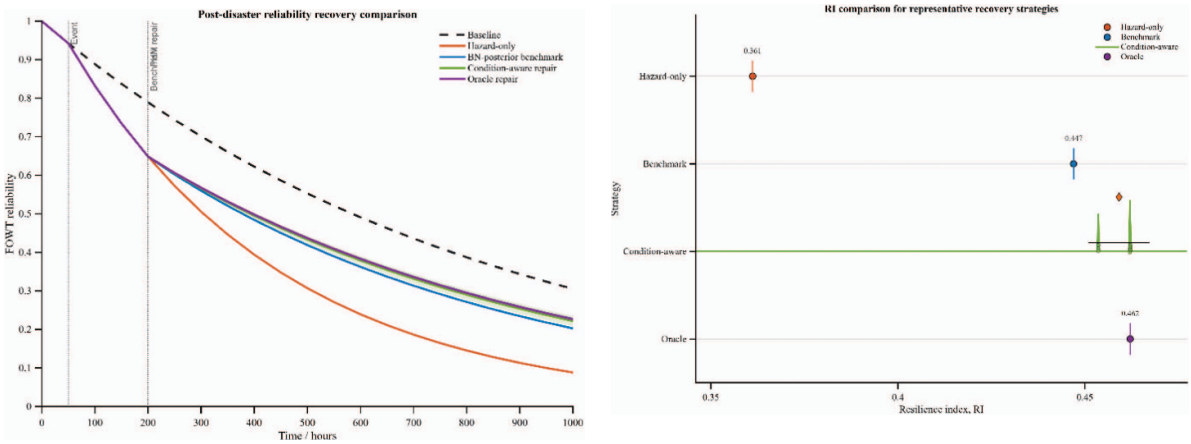
Figure 5 illustrates the influence of PHM diagnostic accuracy on system reliability recovery.

As shown in figure 5(a), increasing diagnostic accuracy moves the condition-aware recovery trajectory closer to the oracle reference, indicating more effective identification of affected root causes and improved repair targeting. This trend is further reflected in figure 5(b), where the mean DRI increases with diagnostic accuracy across all delay levels. However, the benefit of higher accuracy diminishes when diagnostic delay increases, suggesting that accurate diagnosis alone is insufficient if repair actions cannot be implemented in a timely manner.

Figure 6 examines the effect of diagnostic delay on reliability recovery. As shown in figure 6(a), longer delays postpone effective repair actions and result in lower post-disaster reliability recovery. The same trend is observed in figure 6(b), where the mean DRI decreases with increasing diagnostic delay for all accuracy levels. Although higher diagnostic accuracy consistently improves recovery performance, it cannot fully compensate for the negative impact of delayed intervention.

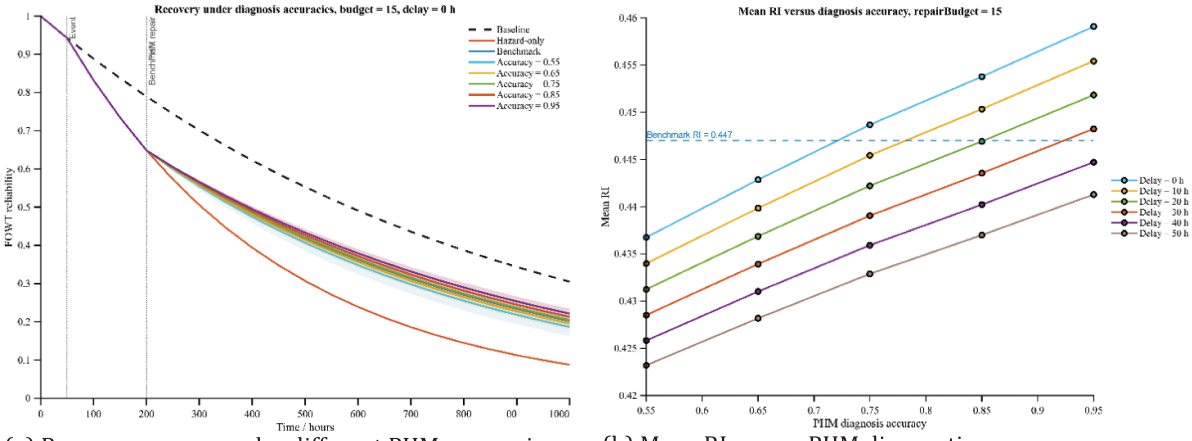
4.3. Interaction effects among accuracy, delay, and budget

Figures 7 and 8 illustrate the interaction among PHM diagnostic accuracy, diagnostic delay, and repair budget from two perspectives of minimum diagnostic accuracy and maximum allowable diagnostic delay, respectively.



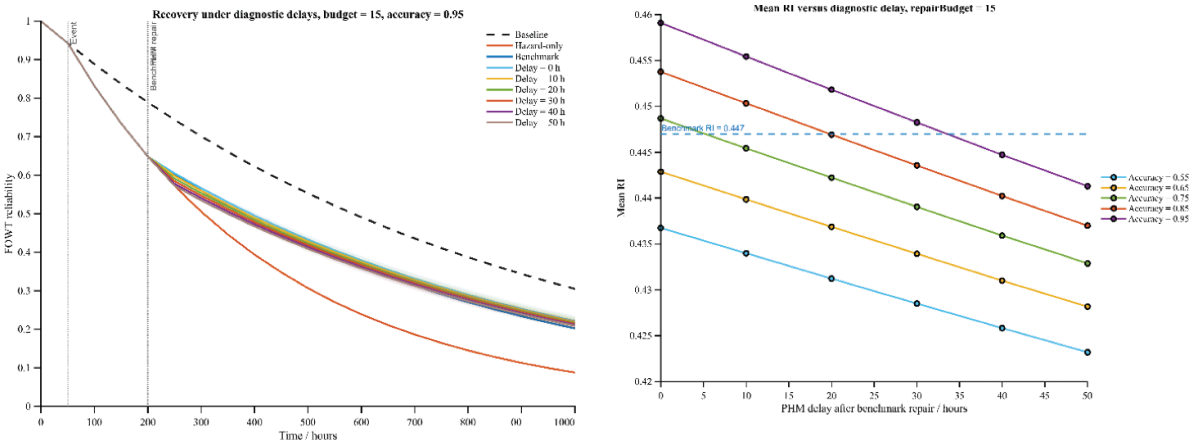
(a) Post-disaster RI curves (b) RI for representative recovery strategies

Figure 4. Comparison of system reliability trajectories and dynamic RI indices under different recovery strategies.



(a) Recovery curves under different PHM accuracies (b) Mean RI versus PHM diagnostic accuracy

Figure 5. Effect of PHM diagnostic accuracy on system reliability recovery and mean dynamic RI.



(a) Recovery curves under different diagnostic delays (b) Mean RI versus diagnostic delay

Figure 6. Effect of diagnostic delay on system reliability recovery and mean dynamic RI.

In figure 7, each cell represents the minimum diagnostic accuracy required for condition-aware recovery to outperform the benchmark strategy under a given combination of repair budget and PHM delay. For example, when the repair budget is 15 and the PHM delay is 30 h, the value of 0.95 means that the diagnostic accuracy must be at least 0.95 for the condition-aware strategy to achieve a positive reliability improvement over the benchmark. If the PHM delay

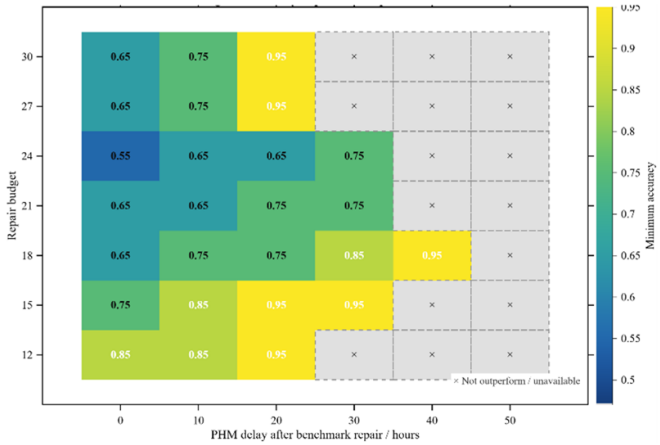


Figure 7. Minimum diagnostic accuracy required for the condition-aware strategy to outperform the benchmark recovery.

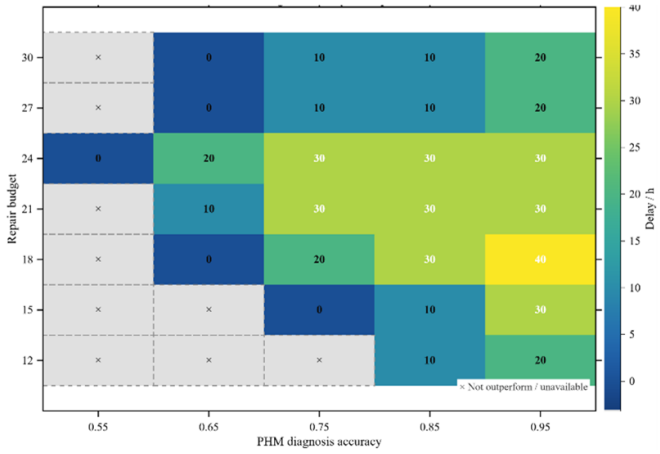


Figure 8. Maximum allowable diagnostic delay for the condition-aware strategy to outperform the benchmark recovery.

increases to 40 h, the same minimum accuracy requirement of 0.95 can only be satisfied with a larger repair budget, such as 18, indicating that additional repair resources are needed to compensate for delayed diagnostic information. Conversely, figure 8 shows the maximum PHM delay that can be tolerated under a given repair budget and diagnostic accuracy while still maintaining a reliability advantage. For instance, when the repair budget is 18 and the diagnostic accuracy is 0.95, the value of 40 h indicates that the condition-aware recovery strategy can tolerate a diagnostic delay of up to 40 h and still outperform the benchmark strategy.

The variation of the threshold values across a row or column should therefore not be interpreted as the effect of a single parameter alone. For example, in the zero-delay column of figure 7, the minimum required accuracy changes with repair budget because each budget level changes the relative recovery performance of both the condition-aware and benchmark strategies. A lower threshold indicates that the condition-aware strategy can outperform the benchmark even with relatively low diagnostic accuracy, whereas a higher threshold means that more accurate PHM information is required to obtain a positive reliability improvement. The results show that diagnostic accuracy, diagnostic delay, and repair budget jointly determine whether condition-aware recovery is beneficial. Limited repair resources restrict the benefit of improved diagnosis, whereas moderate repair budgets allow diagnostic improvements to be translated into more effective reliability recovery. At very high repair budgets, the marginal advantage of condition-aware recovery may decrease because the benchmark strategy also benefits from broader repair coverage. Overall, figures 7 and 8 demonstrate that the effectiveness of condition-aware recovery depends on the combined influence of diagnostic accuracy, diagnostic timeliness, and repair resources rather than any single factor alone.

Figures 9 and 10 further examine the interaction among diagnostic accuracy, diagnostic delay, and repair budget using ΔRI, defined as the difference between the condition-aware RI and the benchmark RI. Positive ΔRI indicates that condition-aware recovery provides a reliability benefit, while negative ΔRI indicates that the additional inspection is not worthwhile. Figure 9 shows that positive ΔRI mainly occurs under high diagnostic accuracy and short-to-moderate diagnostic delay. As accuracy decreases or delay increases, the benefit gradually weakens and may become negative. Figure 10 confirms this trend by reorganizing the results according to diagnostic accuracy. Low accuracy produces limited or negative improvement across most budget-delay combinations, whereas higher accuracy expands the favourable region for condition-aware recovery. Overall, the results indicate that PHM-based recovery is beneficial only within an appropriate accuracy–delay–budget region. High diagnostic accuracy improves both the magnitude and robustness of reliability recovery, but excessive diagnostic delay can still offset this benefit.

Figures 11 and 12 examine the influence of repair budget on the relative reliability improvement, defined as $\Delta\mathrm{RI} = \mathrm{RI}_{\mathrm{phm}} - \mathrm{RI}_{\mathrm{BM}}$. A larger ΔRI therefore indicates a greater advantage of the condition-aware recovery strategy over the benchmark strategy. However, ΔRI is a relative performance measure rather than the absolute reliability achieved by the condition-aware strategy. Therefore, increasing the repair budget does not necessarily lead to a monotonic increase in ΔRI.

As shown in figure 11, the relative improvement generally increases when the repair budget rises from a limited level to a moderate level, indicating that condition-aware recovery can better exploit additional repair resources when the available budget is sufficient to target the diagnosed root causes. For example, several curves show a clear improvement when the budget increases from 15 to 18 or 24. However, when the budget becomes very large, the marginal advantage of condition-aware recovery may decrease. This does not mean that the absolute reliability of the condition-aware strategy deteriorates. Instead, it indicates that the benchmark strategy also benefits from the increased repair budget and can cover a broader set of repair targets, thereby narrowing the performance gap between the two strategies.

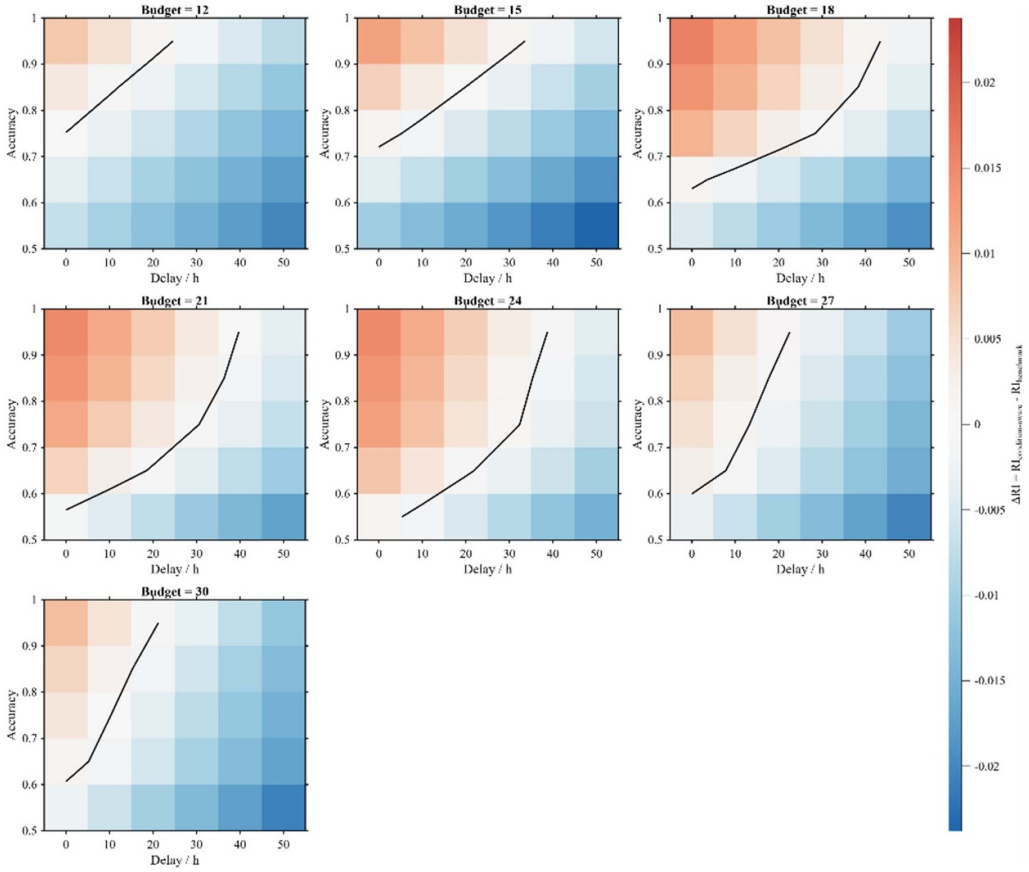


Figure 9. Heatmaps of dynamic RI improvement under varying diagnostic accuracies and delays across different repair budgets.

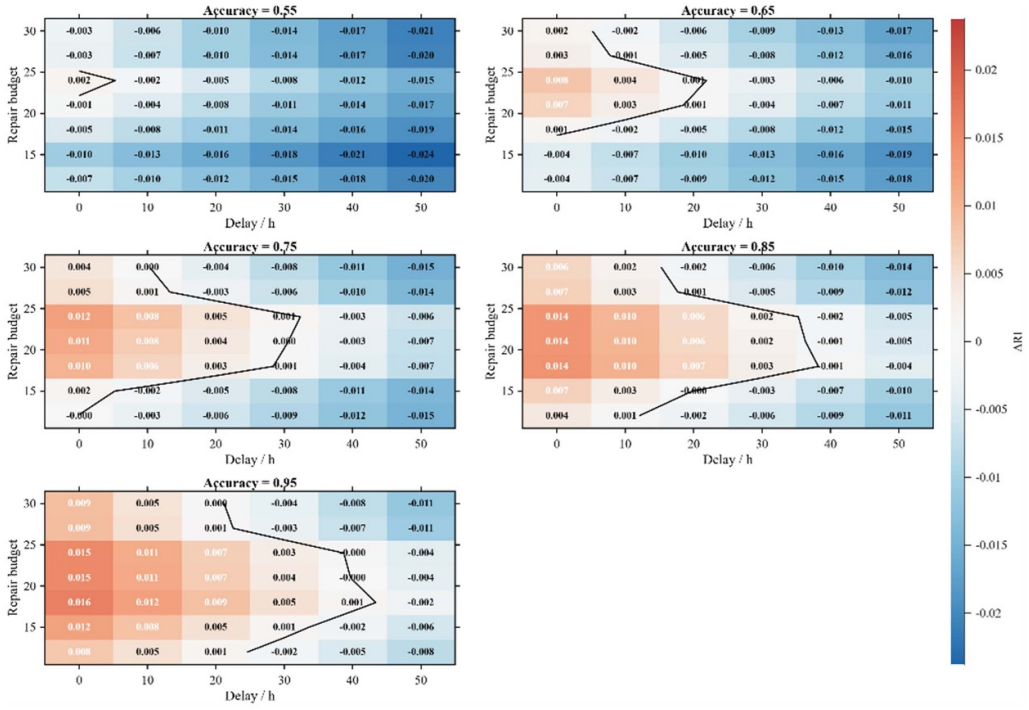


Figure 10. Interaction effects of diagnostic delay and repair budget on dynamic RI improvement at fixed accuracy levels.

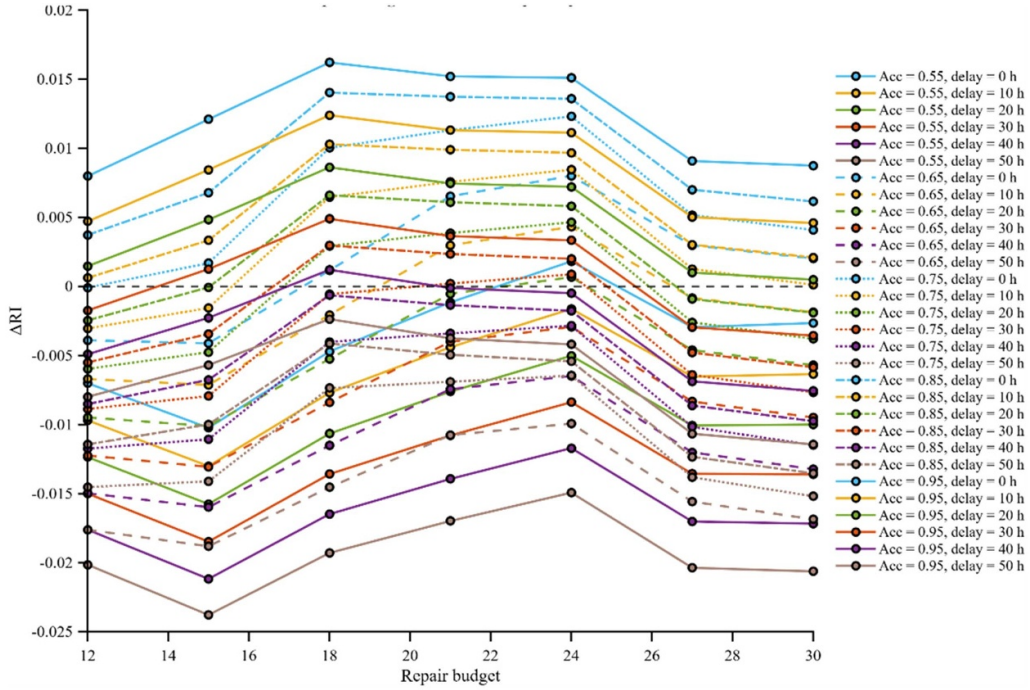


Figure 11. Dynamic RI improvement as a function of repair budget for all accuracy-delay combinations.

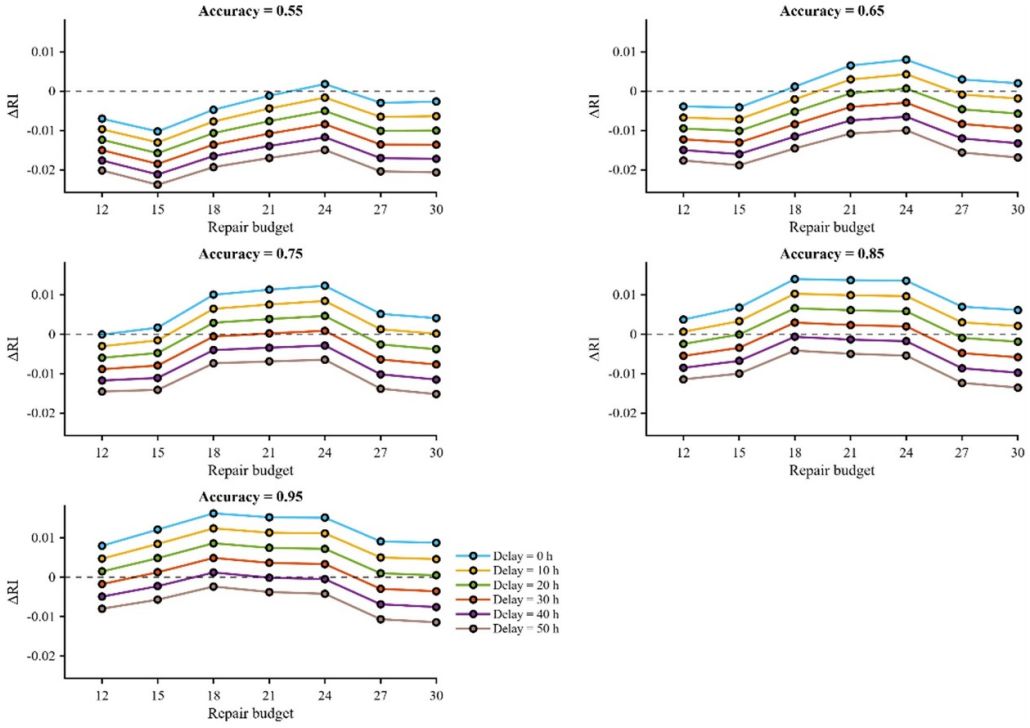


Figure 12. Sensitivity of dynamic RI improvement to repair budget under varying diagnostic delays and fixed accuracy levels.

Figure 12 further separates this budget effect under different diagnostic accuracy levels. At low diagnostic accuracy, additional repair budget provides limited benefit because incorrect or uncertain diagnostic information may prevent the additional resources from being allocated to the true root causes. As diagnostic accuracy increases, condition-aware recovery becomes more effective, especially when the diagnostic delay is short. In these cases, a moderate increase in repair budget can be translated into a larger ΔRI. However, excessive diagnostic delay weakens this advantage because delayed PHM information reduces the timeliness of repair intervention, even when sufficient repair resources are available.

Overall, figures 11 and 12 show that the budget effect on ΔRI is non-monotonic because ΔRI measures the relative advantage over the benchmark, not the absolute reliability level. The results indicate that condition-aware recovery is most beneficial when repair resources are limited to moderate and when diagnostic information is sufficiently accurate and timely. Under very high repair budgets, the benchmark strategy also improves, and the relative advantage of the proposed strategy may consequently decrease.

Overall, figures 7–12 indicate that the value of condition-aware recovery depends on the balance among diagnostic quality, diagnostic timeliness, and repair capacity. The most favourable condition is achieved with high diagnostic accuracy, short-to-moderate delay, and adequate repair budget, whereas low accuracy, excessive delay, or insufficient resources may make condition-aware recovery less effective than benchmark recovery.

4.4. Uncertainty analysis of PHM-enabled risk index

The previous sections mainly focus on mean recovery behaviour and dynamic RI improvement. However, PHM-enabled diagnosis is inherently uncertain. Even under a specified diagnostic accuracy, the identified repair targets may vary across different diagnostic realisations, which leads to uncertainty in the reliability recovery trajectory and the resulting resilience index. Therefore, this section further analyses uncertainty-enabled recovery using fitted reliability distributions.

Figure 13 presents two representative fitted reliability distributions under low and high repair budgets, i.e. Budget = 12 and Budget = 30. The complete fitted reliability distributions under different repair budgets are provided in the appendix. In each subfigure, the panels represent different diagnostic accuracy levels, while the overlaid curves indicate different PHM diagnostic delays. The fitted distributions show that, under the low repair budget, reliability recovery remains limited and uncertain, even when diagnostic accuracy improves. In contrast, under the high repair budget, the distributions shift toward higher local reliability regions and become more concentrated, indicating more effective and stable recovery. The comparison also shows that longer PHM diagnostic delays weaken the recovery benefit, especially by reducing the probability of achieving higher reliability within the selected time nodes.

4.5. Engineering implications for maintenance decision-making

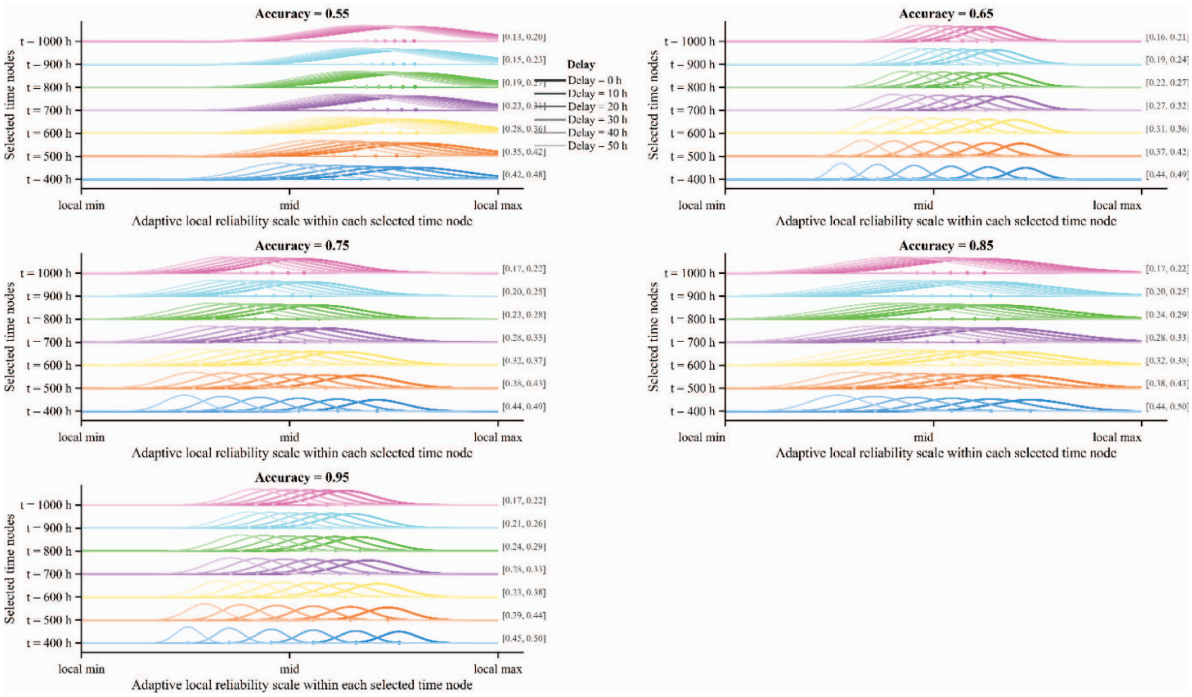
The preceding analyses show that condition-aware recovery can enhance post-disaster dynamic RI, but its benefit depends on diagnostic accuracy, diagnostic delay, repair budget, and uncertainty in root-cause identification. This section translates these findings into engineering implications for post-disaster maintenance decision-making.

Figure 14 compares the dynamic RI distributions under different repair budgets, diagnostic accuracies, and diagnostic delays. Here, D0, D10, D20, D30, D40, and D50 denote diagnostic delays of 0, 10, 20, 30, 40, and 50 h, respectively. The notation D is used only as an abbreviation for delay and does not indicate days. This has been clarified in the revised figure caption. For each repair-budget case, the dashed horizontal line represents the corresponding benchmark RI obtained under the same repair budget. Therefore, the benchmark is not a single fixed value across all subfigures; instead, it is recalculated for each budget level because the benchmark repair strategy also depends on the available repair resources. This allows the condition-aware recovery results to be compared with the appropriate budget-specific benchmark. Values above the dashed line indicate that the condition-aware recovery strategy outperforms the benchmark under the same budget, whereas values below the dashed line indicate that the benchmark strategy performs better. The results show that, under small repair budgets, many condition-aware outcomes remain close to or below the benchmark, indicating that limited repair capacity constrains the benefit of PHM-enabled diagnosis. Under moderate repair budgets, more condition-aware outcomes exceed the benchmark reference, especially when diagnostic accuracy is high and diagnostic delay is short. This suggests that moderate repair capacity provides the most favourable region for translating diagnostic information into effective reliability recovery. Under larger repair budgets, the relative advantage becomes less pronounced because the benchmark strategy also benefits from broader repair coverage. Therefore, repair budget, diagnostic accuracy, and diagnostic delay should be considered jointly rather than independently.

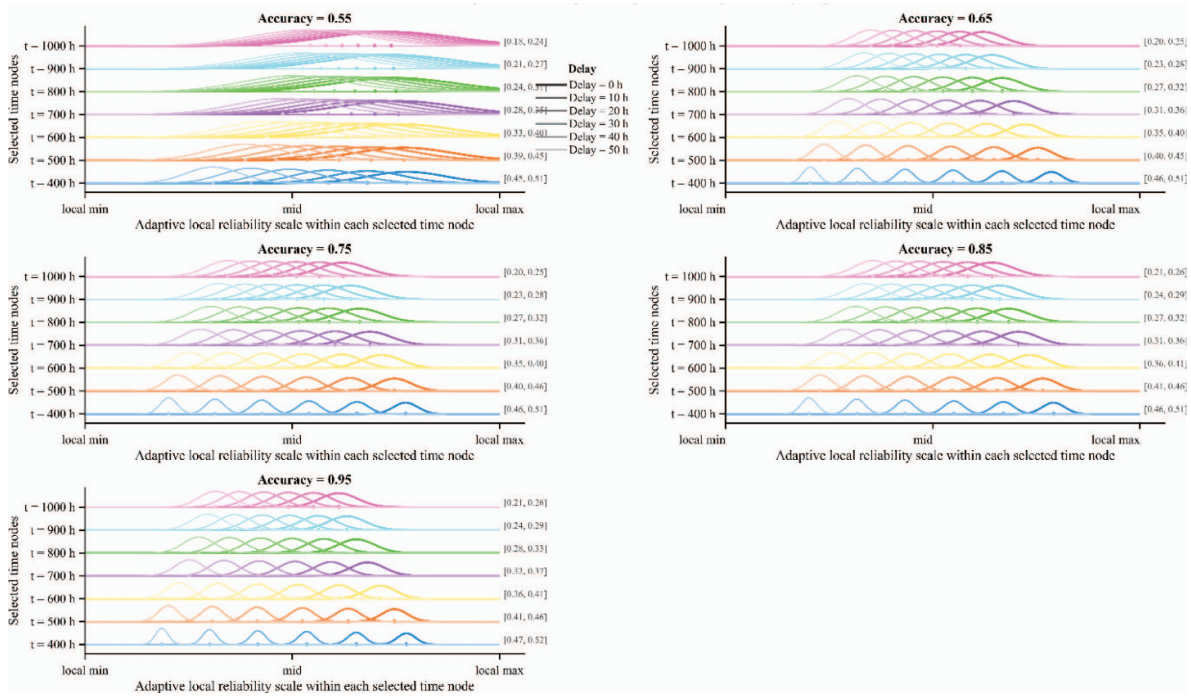
4.6. Sensitivity of hyperparameter

Because the simulation-based resilience framework developed in this study depends on several event-related hyperparameters, a sensitivity analysis was conducted to examine the effects of two key factors on the dynamic RI. The observations of the outcomes from the changes help verify the model, when reflecting the expected values. These factors are the repair rate, which determines how fast a recovery strategy restores the system, and the hazard-induced failure acceleration, which controls the extent to which the hazard increases the root failure rate. In this analysis, only these two factors were varied, while all other model settings were fixed at their baseline values.

Figure 15 compares the dynamic RI under different hazard-induced failure acceleration levels and repair-rate settings. Within the proposed simulation framework, the RI decreases



(a) Budget = 12



(b) Budget = 30

Figure 13. Representative fitted reliability distributions under low and high repair budgets.

monotonically as the hazard intensity scale increases. This behaviour is expected because the hazard intensity scale directly amplifies the root failure rate in the model, leading to faster post-event reliability degradation and hence a lower time-averaged RI over the assessment window. This result should be interpreted as an internal consistency check of the implemented hazard model rather than a universal statement that resilience must always decrease with hazard intensity. In general resilience-curve analysis, stronger disruptions often reduce resilience when they produce larger performance losses, lower residual functionality, or longer recovery durations; however, the final resilience metric also

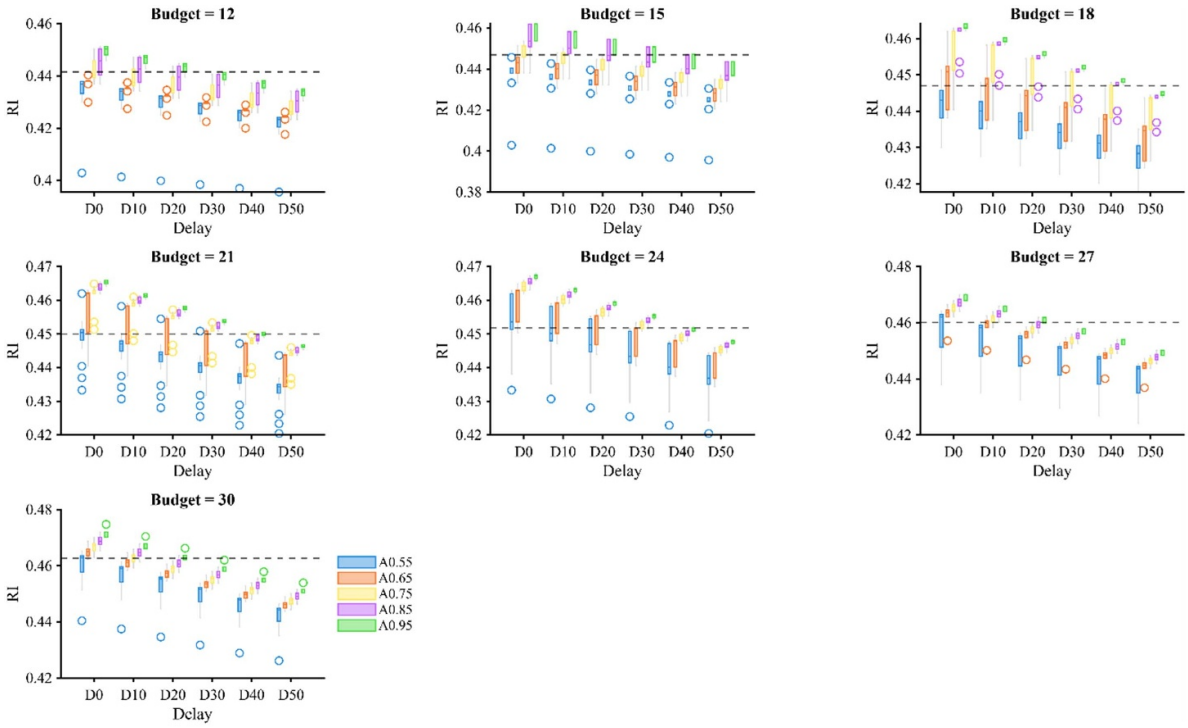


Figure 14. Dynamic RI distributions across varying diagnostic delays and accuracies under different repair budgets.

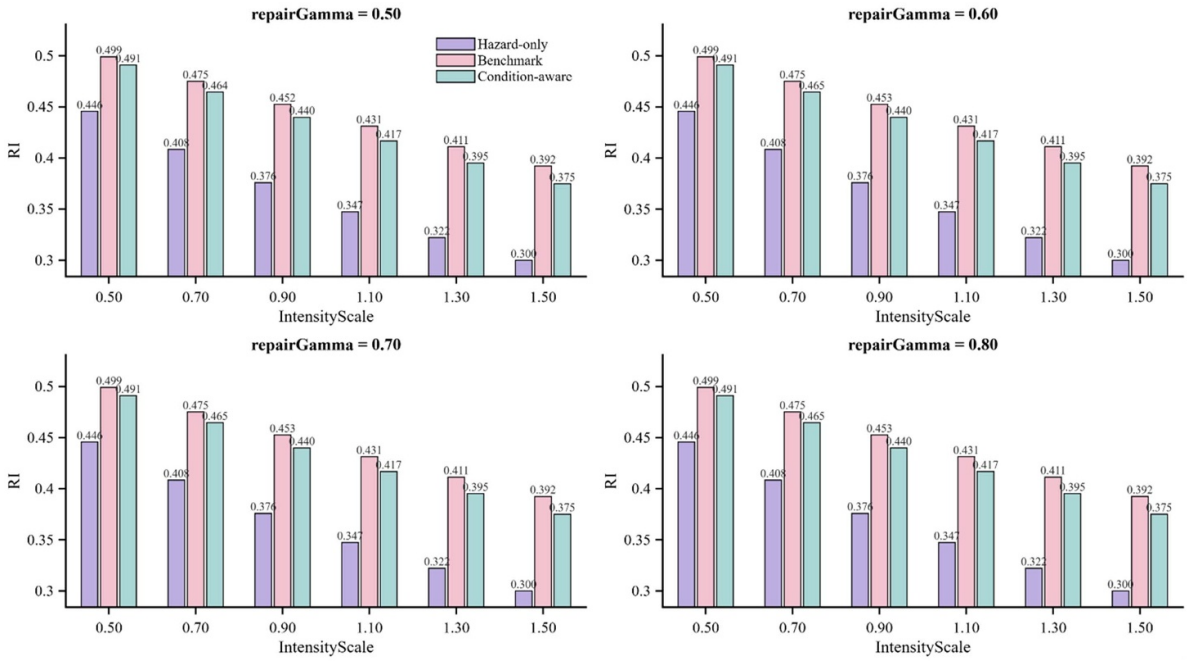


Figure 15. Comparison of the dynamic RI under different hazard-intensity levels for several repair-rate setting.

depends on system redundancy, adaptive capacity, recovery resources, and the definition of the assessment window. Therefore, figure 15 supports the plausibility of the proposed model by showing that the simulated RI responds consistently to the assumed hazard-induced degradation mechanism.

To isolate the influence of the recovery-speed assumption, figure 16 presents a representative comparison in which the hazard intensity is fixed and only the repair rate is varied. In contrast to the strong decreasing trend observed in figure 15, the dynamic RI in figure 16 remains nearly unchanged for all three strategies over the entire tested range. The differences are visually negligible, indicating that moderate changes in the repair-rate setting have only a limited influence on resilience in the present framework.

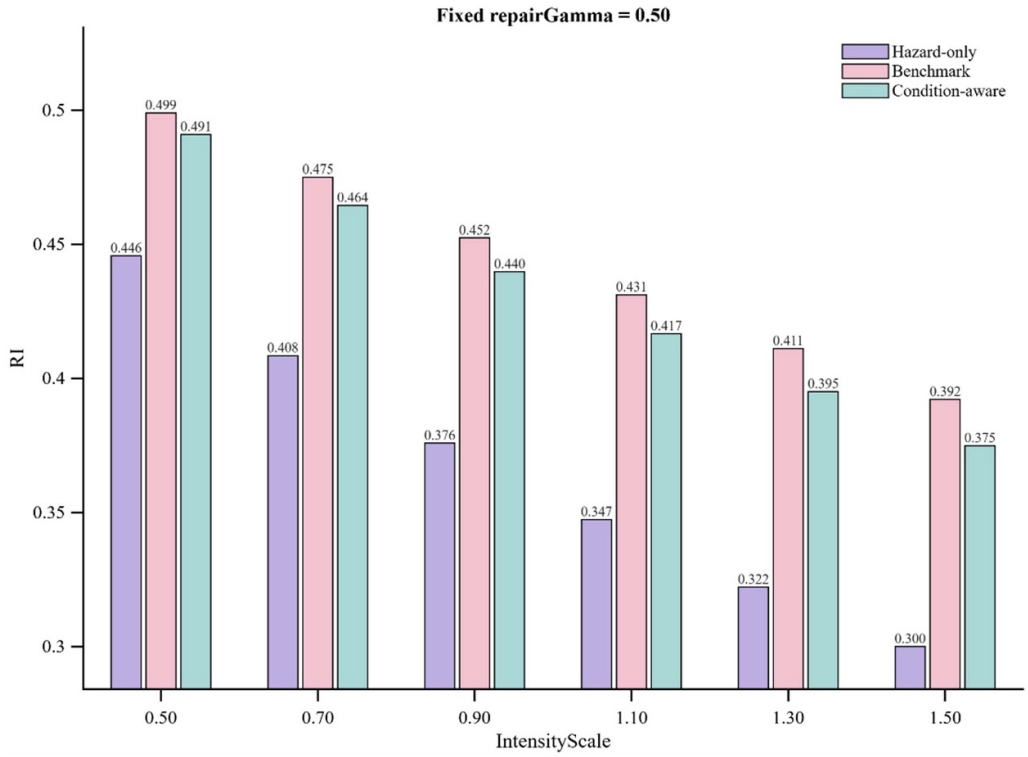


Figure 16. Comparison of the dynamic RI under different repair-rate settings at a fixed hazard-intensity level.

5. Conclusions

This study developed a condition-aware dynamic reliability assessment and recovery decision-making framework for FOWTs under post-disaster recovery scenarios. The proposed framework combines BN-based failure propagation modelling, hazard-induced root-level degradation simulation, diagnosis-informed maintenance decision-making, residual damage modelling, and dynamic RI-based performance quantification. In the framework, a hazardous event affects selected root-level failure causes, whose degradation effects propagate through the BN structure to the subsystem and system levels. During recovery, benchmark recovery, condition-aware recovery, and oracle recovery are compared under different diagnostic accuracies, diagnostic delays, and repair budgets. Dynamic reliability performance is evaluated using reliability recovery trajectories and RI values. The main findings are summarized as follows:

1. Disaster-induced damage at critical root-level failure causes can propagate through the BN structure and lead to clear system-level reliability degradation.
2. The benchmark strategy improves the post-disaster reliability trajectory compared with the hazard-only case, but may miss truly affected root causes and allocate repair resources to incorrect targets, leading to residual degradation after maintenance.
3. The condition-aware strategy achieves better reliability restoration than the benchmark strategy by improving root-cause identification and repair-resource allocation, moving the recovery trajectory closer to the oracle reference.
4. The benefit of condition-aware recovery is not unconditional. Higher diagnostic accuracy improves RI, while longer diagnostic delay reduces this benefit because the system continues to degrade before repair begins. Repair budget further determines whether improved diagnostic information can be converted into actual reliability recovery gains.
5. The uncertainty analysis indicates that PHM-enabled recovery should be interpreted as a probabilistic process rather than a deterministic improvement. Diagnostic uncertainty can lead to different repair targets and recovery trajectories. Therefore, PHM information should be evaluated together with accuracy, delay, and repair-resource constraints.

Overall, the proposed framework provides an interpretable decision-support tool for evaluating post-disaster reliability degradation and recovery strategies of FOWTs. It highlights that effective resilience improvement should not only focus on restoring observable abnormal states, but also identify and repair hidden root causes to reduce residual degradation.

From a practical perspective, the proposed framework provides several implications for future offshore wind farm operation and maintenance. First, since the recovery performance is highly dependent on root-cause failure identification, more effective sensor deployment strategies and reliable monitoring systems are required to capture degradation information associated with critical root failures. Second, the results

highlight the importance of developing root-failure-oriented PHM methods capable of identifying underlying failure mechanisms rather than merely detecting abnormal symptoms from SCADA data. Such capabilities can improve maintenance targeting and reduce residual damage after repair.

Future research will focus on developing more comprehensive resilience indicators that extend beyond reliability alone, thereby enabling a more systematic evaluation of the resilience of FOWTs under hazardous conditions.

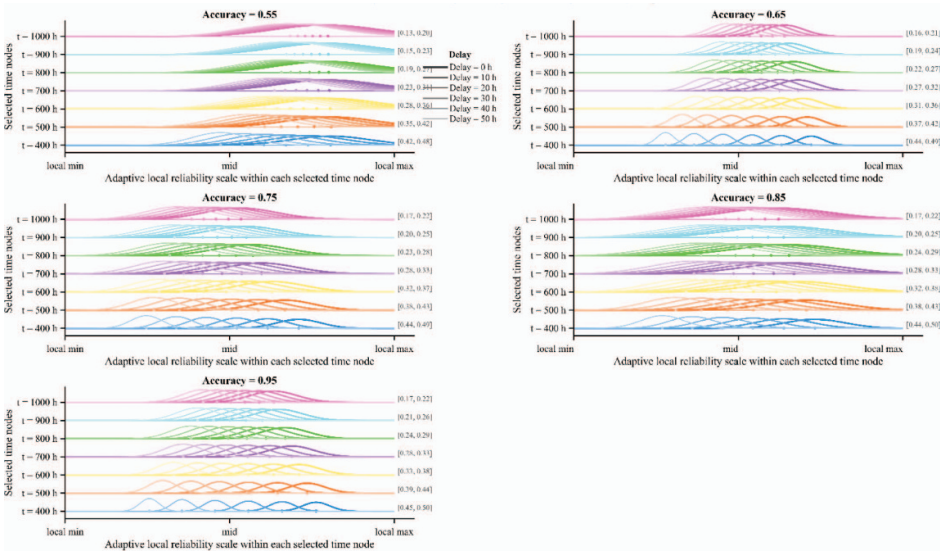
Acknowledgments

This research was funded by the European Research Council (ERC) under the European Union's Horizon 2020 research and innovation programme, Grant Agreement No. 864724; the National Natural Science Foundation of China, Grant No. 52506259; the Natural Science Foundation of Shanghai Municipality, Grant No. 24ZR1454800; and the State Key Laboratory of Mechanical System and Vibration, Grant No. MSV202411.

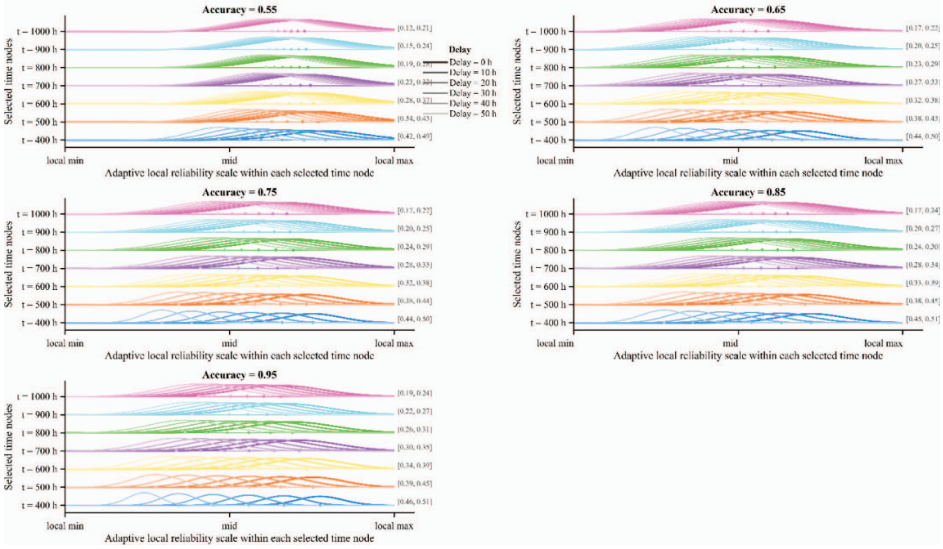
Appendix

The complete fitted reliability distributions for all repair budgets are presented in figure 17. The overall trends are consistent with those discussed in section 4.4. Increasing repair budget generally shifts the reliability distributions towards higher reliability regions and reduces recovery uncertainty, while longer PHM delays reduce the probability of favourable recovery outcomes.

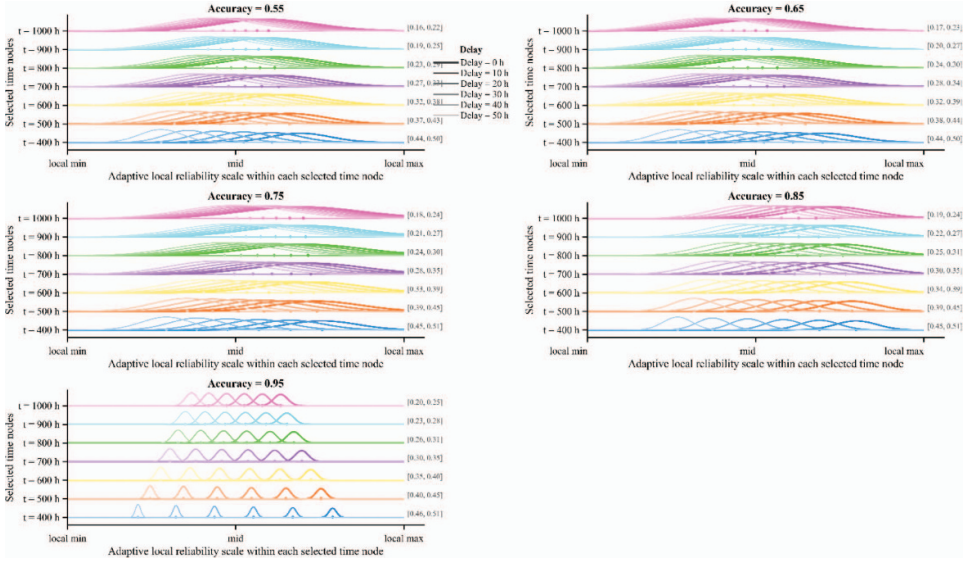
Table 7 records the selected roots, the truly affected roots among them, the missed affected roots, and the unnecessary repair targets.



(a) Budget = 12

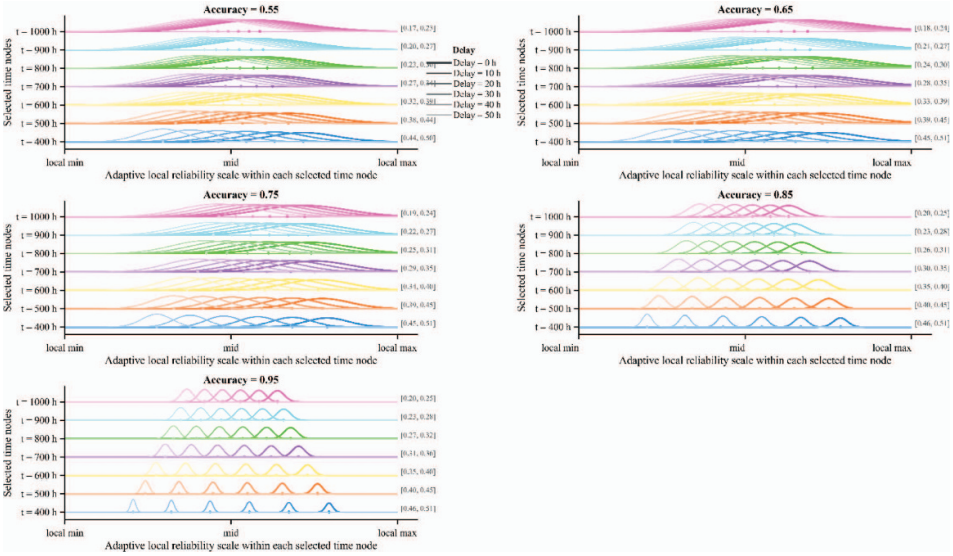


(b) Budget = 15

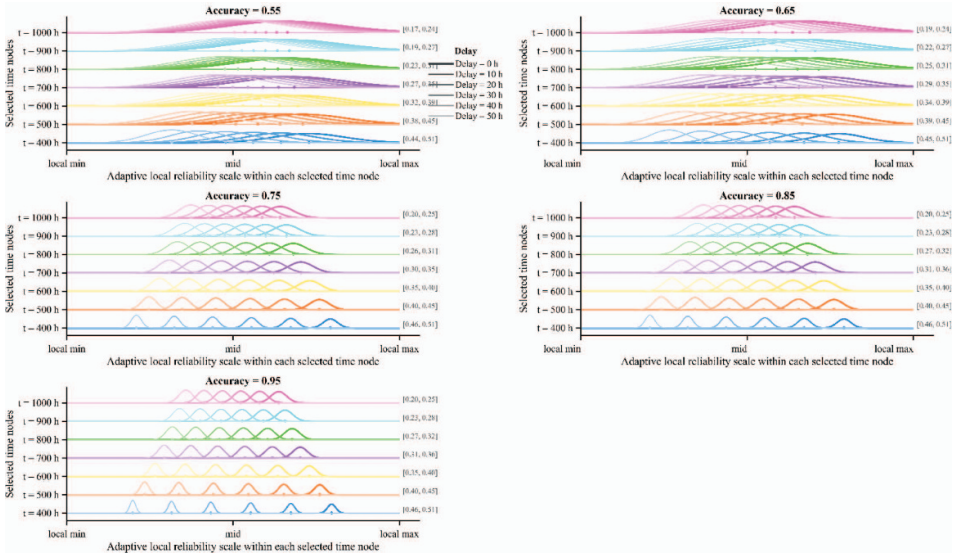


(c) Budget = 18

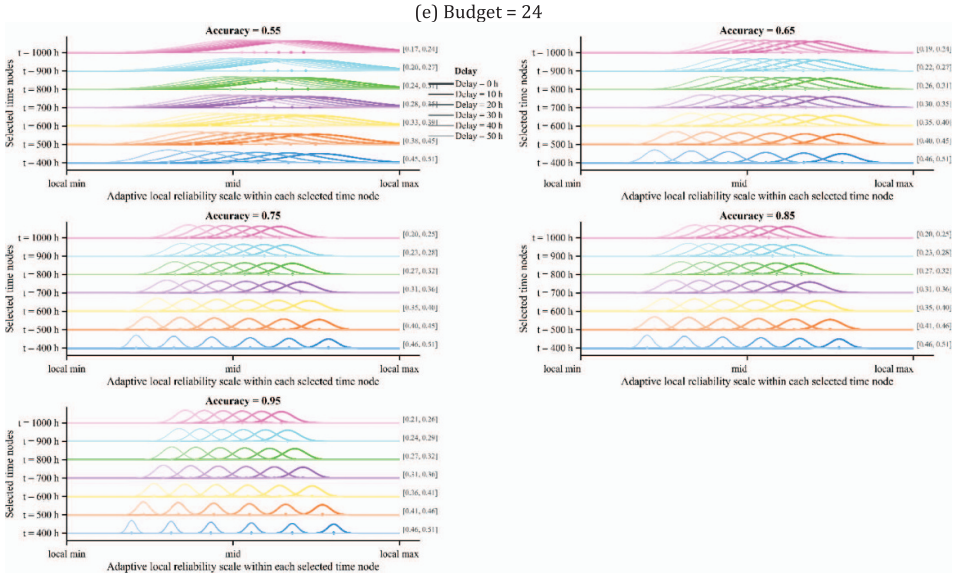
Figure 17. Complete fitted reliability distributions under different repair budgets.



(d) Budget = 21

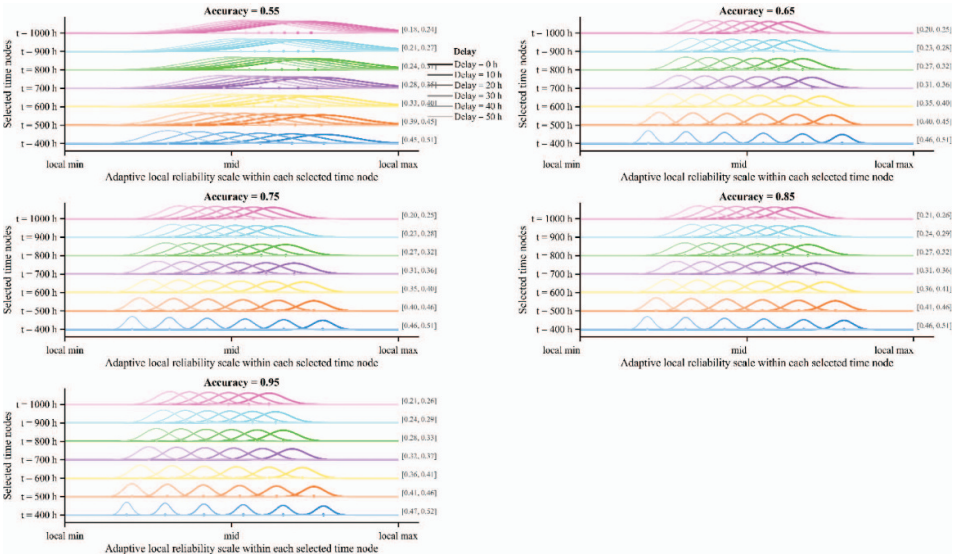


(e) Budget = 24



(f) Budget = 27

Figure 17. (Continued.)



(g) Budget = 30

Figure 17. (Continued.)

Table 7. Detailed benchmark repair targets and outcomes.

Repair budget	Benchmark repair targets	Correctly repaired roots	Missed affected roots	Wrong repair target
12	B10, B11, B12, B13, B14, B15, B26, B06, B07, B08, B09, B27	B10, B11, B12, B13, B14, B15, B26, B06, B07, B08, B09, B27	B29, B30, B31, B78, B28, B79, B80, B22, B23, B25, B16, B24, B20, B21, B47, B64, B71, B76	N/A
15	B10, B11, B12, B13, B14, B15, B26, B06, B07, B08, B09, B27, B28, B02, B03	B10, B11, B12, B13, B14, B15, B26, B06, B07, B08, B09, B27, B28	B29, B30, B31, B78, B79, B80, B22, B23, B25, B16, B24, B20, B21, B47, B64, B71, B76	B02, B03
18	B10, B11, B12, B13, B14, B15, B26, B06, B07, B08, B09, B27, B28, B02, B03, B04, B05, B01	B10, B11, B12, B13, B14, B15, B26, B06, B07, B08, B09, B27, B28	B29, B30, B31, B78, B79, B80, B22, B23, B25, B16, B24, B20, B21, B47, B64, B71, B76	B02, B03, B04, B05, B01
21	B10, B11, B12, B13, B14, B15, B26, B06, B07, B08, B09, B27, B28, B02, B03, B04, B05, B01, B20, B21, B22	B10, B11, B12, B13, B14, B15, B26, B06, B07, B08, B09, B27, B28, B20, B21, B22	B29, B30, B31, B78, B79, B80, B23, B25, B16, B24, B47, B64, B71, B76	B02, B03, B04, B05, B01
24	B10, B11, B12, B13, B14, B15, B26, B06, B07, B08, B09, B27, B28, B02, B03, B04, B05, B01, B20, B21, B22, B23, B24, B25	B10, B11, B12, B13, B14, B15, B26, B06, B07, B08, B09, B27, B28, B20, B21, B22, B23, B24, B25	B29, B30, B31, B78, B79, B80, B16, B47, B64, B71, B76	B02, B03, B04, B05, B01
27	B10, B11, B12, B13, B14, B15, B26, B06, B07, B08, B09, B27, B28, B02, B03, B04, B05, B01, B20, B21, B22, B23, B24, B25, B78, B79, B80	B10, B11, B12, B13, B14, B15, B26, B06, B07, B08, B09, B27, B28, B20, B21, B22, B23, B24, B25, B78, B79, B80	B29, B30, B31, B16, B47, B64, B71, B76	B02, B03, B04, B05, B01
30	B10, B11, B12, B13, B14, B15, B26, B06, B07, B08, B09, B27, B28, B02, B03, B04, B05, B01, B20, B21, B22, B23, B24, B25, B78, B79, B80, B74, B75, B76	B10, B11, B12, B13, B14, B15, B26, B06, B07, B08, B09, B27, B28, B20, B21, B22, B23, B24, B25, B78, B79, B80, B76	B29, B30, B31, B16, B47, B64, B71	B02, B03, B04, B05, B01, B74, B75

References

[1] Jonasson E, Forsberg S, Jurasz J, Canales F A and Temiz I 2026 Global techno-economic assessment of hybrid offshore wind, wave, and solar power *Appl. Energy* **415** 127880

[2] Li H, Díaz H and Guedes Soares C 2021 A failure analysis of floating offshore wind turbines using AHP-FMEA methodology *Ocean Eng.* **234** 109261

[3] Stankovic A M 2023 Methods for analysis and quantification of power system resilience *IEEE Trans. Power Syst.* **38** 4774–87

[4] Li H, Huang C-G and Soares C G 2022 A real-time inspection and opportunistic maintenance strategies for floating offshore wind turbines *Ocean Eng.* **256** 111433

[5] Li H, Ding Y, Sun Y, Xie M and Guedes Soares C 2025 An intelligent failure feature learning method for failure and maintenance data management of wind turbines *Reliab. Eng. Syst. Saf.* **261** 111113

[6] Song Y and Li R 2022 System resilience distribution identification and analysis based on performance processes after disruptions *PLoS One* **17** e0276908

[7] Dui H, Lu Y and Wu S 2024 Competing risks-based resilience approach for multi-state systems under multiple shocks *Reliab. Eng. Syst. Saf.* **242** 109773

[8] Hoseyni S M and Cordiner J 2024 A novel framework for quantitative resilience assessment in complex engineering systems during early and late design stages *Process Safety Environ. Prot.* **189** 612–27

[9] Rathnayaka B, Robert D, Adikariwattage V, Siriwardana C, Meegahapola L, Setunge S and Amaratunga D 2024 A unified framework for evaluating the resilience of critical infrastructure: Delphi survey approach *Int. J. Disaster Risk Reduct.* **110** 104598

[10] Firoozi A A, Firoozi A A, Alashker Y and Ahmad S 2024 Advancing civil engineering: the transformative impact of neuromorphic computing on infrastructure resilience and sustainability *Results Eng.* **24** 103487

[11] Wu X, Zhao Y, Wang D, Huang J and Zheng K 2026 Resilience assessment of power distribution systems based on structure varied dynamic Bayesian network under rainstorm disasters *Reliab. Eng. Syst. Saf.* **266** 111660

[12] Zhang J, Xin X, Dubey R, Nguyen T T, Shi X, Li N and Yang Z 2025 Impact of the ripple effect on the resilience of multimodal container port operations: a system dynamics simulation approach *Risk Anal.* **45** 4903–32

[13] Poulin C and Kane M B 2021 Infrastructure resilience curves: performance measures and summary metrics *Reliab. Eng. Syst. Saf.* **216** 107926

[14] Linkov I, Trump B D, Trump J, Pescaroli G, Hynes W and Mavrodieva A and Panda A 2022 Resilience stress testing for critical infrastructure *Int. J. Disaster Risk Reduct.* **82** 103323

[15] Yang H, Liu C, Cao Y, Shu Y, Gan L, Liu Z and Yang Z 2026 Dynamic resilience assessment of global shipping networks against cascading effects: an AIS data-driven complex network analysis *Sustain. Horiz.* **18** 100184

[16] Amlashi H and Karimirad M 2025 Fatigue reliability assessment of floating and bottom-fixed offshore wind turbines *ASME 44th Int. Conf. on Ocean, Offshore and Arctic Engineering* (https://doi.org/10.1115/OMAE2025-156360)

[17] Ren C and Xing Y 2025 Active learning with a multi-point enrichment strategy for multi-location fatigue assessment of offshore wind turbines *Eng. Struct.* **336** 120344

[18] Ren C and Xing Y 2024 An efficient active learning Kriging approach for expected fatigue damage assessment applied to wind turbine structures *Ocean Eng.* **305** 118034

[19] Yuan Y, Dong Y, Zhang J and Yan B 2026 Probabilistic vulnerability assessment of floating offshore wind turbines under typhoon hazards considering long-term corrosion–fatigue degradation *Eng. Struct.* **357** 122577

[20] Xie W, Zhou X, Ke K, Yam M C H and Yan Y 2026 A resilient jacket-type offshore wind turbine system: conception, surrogate-integrated modelling, and seismic performance evaluation *Ocean Eng.* **349** 124123

[21] Sahu S K, Kumar V, Chandra Dutta S, Sarkar R, Bhattacharya S and Debnath P 2024 Structural safety of offshore wind turbines: present state of knowledge and future challenges *Ocean Eng.* **309** 118383

[22] Yi M S, Lee D H and Park J S 2026 Towards adaptive collision energy standards for offshore jack-up legs: a structural failure mechanics perspective *Appl. Ocean Res.* **166** 104900

[23] Chen B Q, Liu K, Rong H and Ringsberg J W 2026 Ship collision and offshore renewable energy: challenges and innovations for structural resilience *Renew. Sustain. Energy Rev.* **226** 116510

[24] Song Y, Hong X, Zhang Z, Sun T and Cai Y 2025 Reliability analysis of floating offshore wind turbine considering multiple failure modes under extreme typhoon-wave condition *Ocean Eng.* **323** 120564

[25] Zhang J, Shittu A A, Chujutalli J H, Amiri M M, Shadman M, An C and Levi C 2026 Reliability assessment for sub-structure of concrete floating offshore wind turbine platforms under ultimate limit state *Ocean Eng.* **343** 123326

[26] Zhou D, Pan X, Guo J, Sun X, Wang C and Zheng J 2025 Resilience quantification of offshore wind farm cluster under the joint influence of typhoon and its secondary disasters *Appl. Energy* **383** 125323

[27] Wu J and Guedes Soares C 2026 Multi-dimensional resilience modelling framework for offshore wind farms under operational and extreme disruptions *Renew. Sustain. Energy Rev.* **230** 116667

[28] Rajabi M, Hajibabaei M, Dastgir A and Sitzenfrei R 2026 Functional and structural resilience assessment in urban drainage networks: a physics-guided graph-based surrogate model *Water Res.* **289** 124784

[29] Wang N, Wu M and Yuen K F 2025 Dynamic enterprise resilience assessment for port systems: a framework integrating Bayesian networks and Dempster-Shafer evidence theory *Reliab. Eng. Syst. Saf.* 262

[30] Yang Z, Lau Y-Y, Poo M C-P, Yin J and Yang Z 2025 Port resilience to climate change in the greater Bay area *Transp. Res. D* **142** 104681

[31] Chang Z, Suo M, Fan H, Wang J and Lai W 2025 Port resilience assessment under congestion disruptions *J. Sea Res.* **207** 102611

[32] Peng C, Zhen X and Huang Y 2023 A structured approach for resilience-oriented human performance assessment and prediction in offshore safety-critical operations *Ocean Eng.* **287** 115743

[33] Wu J, Yu Y, Jin Z and Zhang W 2024 Multi-dimensional resilience assessment framework of offshore structure under mooring failure *Reliab. Eng. Syst. Saf.* **247** 110108

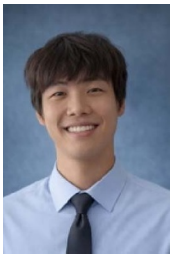
[34] Yu Y, Zhang W, Zhang B and Wu J 2024 Reliability-based resilience assessment method for mooring systems under mooring failure *Earthq. Eng. Resilience* **3** 191–218

[35] Rezende F A, Videiro P M, Sagrilo L V S and Oliveira M C 2024 Reliability-based fatigue inspection planning for mooring chains of floating systems *Reliab. Eng. Syst. Saf.* **242** 109775

[36] Xu Z 2025 An intelligent predictive maintenance framework for floating offshore wind turbine based on structural damage prediction *Appl. Ocean Res.* **164** 104796

[37] Göteman M, Panteli M, Rutgersson A, Hayez L, Virtanen M J, Anvari M and Johansson J 2025 Resilience of offshore

renewable energy systems to extreme metocean conditions: a review *Renew. Sustain. Energy Rev.* **216** 115649
[38] Nguyen H T, Muhs J W and Parvania M 2019 Assessing impacts of energy storage on resilience of distribution systems against hurricanes *J. Mod. Power Syst. Clean Energy* **7** 731–40
[39] Ghasemi S and Moshtagh J 2022 Distribution system restoration after extreme events considering distributed generators and static energy storage systems with mobile energy storage systems dispatch in transportation systems *Appl. Energy* **310** 118507
[40] Liu Y, Ma X, Qiao W, Ma L and Han B 2024 A novel methodology to model disruption propagation for resilient maritime transportation systems–a case study of the Arctic maritime transportation system *Reliab. Eng. Syst. Saf.* **241** 109620
[41] Dui H, Zheng X and Wu S 2021 Resilience analysis of maritime transportation systems based on importance measures *Reliab. Eng. Syst. Saf.* **209** 107461
[42] Dong B X, Shan M and Hwang B G 2022 Simulation of transportation infrastructures resilience: a comprehensive review *Environ. Sci. Pollut. Res.* **29** 12965–83
[43] Kammouh O, Gardoni P and Cimellaro G P 2020 Probabilistic framework to evaluate the resilience of engineering systems using Bayesian and dynamic Bayesian networks *Reliab. Eng. Syst. Saf.* **198** 106813
[44] Li H, Guedes Soares C and Huang H Z 2020 Reliability analysis of a floating offshore wind turbine using Bayesian networks *Ocean Eng.* **217** 107827
[45] Li H and Guedes Soares C 2022 Assessment of failure rates and reliability of floating offshore wind turbines *Reliab. Eng. Syst. Saf.* **228** 108777
[46] Li J, Li Z, Jiang Y and Tang Y 2022 Typhoon resistance analysis of offshore wind turbines: a review *Atmosphere* **13** 451
[47] Sun Y, Li H, Sun L and Guedes Soares C 2023 Failure analysis of floating offshore wind turbines with correlated failures *Reliab. Eng. Syst. Saf.* **238** 109485
[48] Shafiee M 2023 Failure analysis of spar buoy floating offshore wind turbine systems *Innov. Infrastruct. Solut.* **8** 28
[49] Zhang Z, Wang X, Zhang X, Zhou C and Wang X 2024 Dynamic responses and mooring line failure analysis of the fully submersible platform for floating wind turbine under typhoon *Eng. Struct.* **301** 117334
[50] Melchers R E and Beck A T 2017 *Structural Reliability Analysis and Prediction* (Wiley) (https://doi.org/10.1002/9781119266105)
[51] Chen X, Li C and Xu J 2015 Failure investigation on a coastal wind farm damaged by super typhoon: a forensic engineering study *J. Wind Eng. Ind. Aerodyn.* **147** 132–42
[52] Faulstich S, Hahn B, Lyding P and Tavner P J 2009 Reliability of offshore turbines—identifying risks by onshore experience *European Offshore Wind Conference* https://durham-repository.worktribe.com/output/1160225
[53] Chen B, Tavner P J, Feng Y, Song W W and Qiu Y n.d. Bayesian networks for wind turbine fault diagnosis *EWEA 2012* (*Copenhagen, Denmark.*) http://proceedings.ewea.org/annual2012/proceedings/#
[54] Adedipe T, Shafiee M and Zio E 2020 Bayesian network modelling for the wind energy industry: an overview *Reliab. Eng. Syst. Saf.* **202** 107053
[55] Dao C D, Kazemtabrizi B, Crabtree C J and Tavner P J 2021 Integrated condition-based maintenance modelling and optimisation for offshore wind turbines *Wind Energy* **24** 1180–98
[56] Kang J, Sobral J and Soares C G 2019 Review of condition-based maintenance strategies for offshore wind energy *J. Mar. Sci. Appl.* **18** 1–16
[57] Plumley C E, Wilson G K, Kenyon A D and Zitrou A n.d. Diagnostics and prognostics utilising dynamic Bayesian networks applied to a wind turbine gearbox *Int. Conf. on Condition Monitoringand Machine Failure Prevention Technologies*
[58] Liang H, Moya B, Chinesta F, Chatzi E, Liang H and Moya B 2025 Resilience-based post disaster recovery optimization for infrastructure system via deep reinforcement learning Rights/license: creative Commons Attribution 4.0 International (https://doi.org/10.3929/ethz-c-000782743)
[59] Liang H, Moya B, Chinesta F and Chatzi E 2025 Resilience-based post disaster recovery optimization for infrastructure system via deep reinforcement learning
[60] Liang H, Moya B, Chinesta F and Chatzi E 2026 Resilience-based post disaster recovery optimization for infrastructure system via deep reinforcement learning *Reliab. Eng. Syst. Saf.* **265** 111478



Dr Zifei Xu is a School Research Fellow at Liverpool John Moores University and is affiliated with the Department of Civil and Environmental Engineering at the University of Liverpool. He was awarded a Marie Skłodowska-Curie Fellowship in 2022. His research interests include predictive maintenance and resilient infrastructure.



Mr Huahao Ou is a PhD candidate in the Department of Power Engineering at the University of Shanghai for Science and Technology. His research focuses on the application of computational mechanics to wind turbine blade performance monitoring and optimization.



Professor Musa Bashir is the Chair of Maritime Engineering and Director of Postgraduate Research Studies at the University of Liverpool. His research interests include renewable energy systems, offshore structures, integrity management, and AI-enabled predictive maintenance for maritime and offshore engineering.



Professor Michael Beer is Professor and Head of the Institute for Risk and Reliability at Leibniz University Hannover, Germany, and Professor of Uncertainty in Engineering at the University of Liverpool, UK. He is President-elect of the International Association for Structural Safety and Reliability (IASSAR) and Chair of the European Safety and Reliability Association.



Professor Jin Wang is Professor of Marine Technology at Liverpool John Moores University and Director of the Liverpool Logistics, Offshore and Marine Research Institute. He is an elected Member of the European Academy of Sciences. His research focuses on marine safety, risk assessment, reliability engineering, and intelligent maritime systems.



Professor Zaili Yang is Professor of Maritime Transport and Co-Director of the Liverpool Logistics, Offshore and Marine Research Institute (LOOM) at Liverpool John Moores University. He is the recipient of a prestigious European Research Council (ERC) Consolidator Grant and has led numerous international research projects in maritime transport, logistics, and risk and resilience engineering.